

Mechanical characterization of nanopillars by atomic force microscopy

Angeloni, L.; Ganjian, M.; Nouri-Goushki, M.; Mirzaali, M. J.; Hagen, C. W.; Zadpoor, A. A.; Fratila-Apachitei, L. E.; Ghatkesar, M. K.

DOI

[10.1016/j.addma.2021.101858](https://doi.org/10.1016/j.addma.2021.101858)

Publication date

2021

Document Version

Final published version

Published in

Additive Manufacturing

Citation (APA)

Angeloni, L., Ganjian, M., Nouri-Goushki, M., Mirzaali, M. J., Hagen, C. W., Zadpoor, A. A., Fratila-Apachitei, L. E., & Ghatkesar, M. K. (2021). Mechanical characterization of nanopillars by atomic force microscopy. *Additive Manufacturing*, 39, Article 101858. <https://doi.org/10.1016/j.addma.2021.101858>

Important note

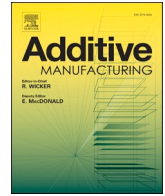
To cite this publication, please use the final published version (if applicable).
Please check the document version above.

Copyright

Other than for strictly personal use, it is not permitted to download, forward or distribute the text or part of it, without the consent of the author(s) and/or copyright holder(s), unless the work is under an open content license such as Creative Commons.

Takedown policy

Please contact us and provide details if you believe this document breaches copyrights.
We will remove access to the work immediately and investigate your claim.



Research Paper

Mechanical characterization of nanopillars by atomic force microscopy

L. Angeloni^{a,b,*}, M. Ganjian^b, M. Nouri-Goushki^b, M.J. Mirzaali^b, C.W. Hagen^c, A.A. Zadpoor^b,
L.E. Fratila-Apachitei^{b,1}, M.K. Ghatkesar^{a,**,1}

^a Department of Precision and Microsystems Engineering, Faculty of Mechanical, Maritime, and Materials Engineering, Delft University of Technology, Mekelweg 2, Delft 2628CD, The Netherlands

^b Department of Biomechanical Engineering, Faculty of Mechanical, Maritime, and Materials Engineering, Delft University of Technology, Mekelweg 2, Delft 2628CD, The Netherlands

^c Department of Imaging Physics, Faculty of Applied Sciences, Delft University of Technology, Lorentzweg 1, Delft 2628CJ, The Netherlands

ARTICLE INFO

Keywords:

Atomic force microscopy
Contact mode
Force spectroscopy
Nanopillars
Nanomechanics
Nanomechanical characterization

ABSTRACT

Micro- and nano-patterns are gaining increasing attraction in several fields ranging from nanoelectronics to bioengineering. The mechanical properties of the nanostructures (nanopillars, nanotubes, nanowires, etc.) are highly relevant for many applications but challenging to determine. Existing mechanical characterization methods require mounting the testing setup inside a scanning electron microscope (SEM) and additional sample modification. Here, we propose two atomic force microscopy (AFM) methods, based on contact mode imaging (CMI) and force spectroscopy imaging (FSI), to determine the mechanical characteristics of individual micro- and nanopillars as fabricated, without using SEM. We present the working principles of both methods and two case studies on nanopillars fabricated by additive manufacturing methods: two-photon polymerization (2PP) and electron beam induced deposition (EBID). Various mechanical parameters were determined using CMI and FSI, respectively. For the 2PP nanopillars, we measured the stiffness (13.5 ± 3.2 N/m and 15.9 ± 2.6 N/m), the maximum lateral force (883.0 ± 89.5 nN and 889.6 ± 113.6 nN), the maximum deflection (64.2 ± 13.6 nm and 58.3 ± 14.24 nm), the failure stress (0.3 ± 0.03 GPa and 0.3 ± 0.02 GPa), and the adhesion force (56.6 ± 4.5 μN and 58.6 ± 5.2 μN). For the EBID nanopillars, we measured the failure stress (2.9 ± 0.2 GPa and 2.7 ± 0.4 GPa). The similar results obtained using both techniques confirmed the efficacy and consistency of the methods. The proposed methodologies have the potential of enabling otherwise impossible measurements particularly when the specimens need to be tested under wet conditions, such as patterns for mechanobiological studies.

1. Introduction

Patterning strategies at the micro- and nano-scale are receiving increased attention because of their many applications in diverse fields, including nanoelectronics [1], nanoenergy [2], microfluidics [3], mechanics [4,5], and bioengineering [6–8].

Among the different technological area, surface patterning is showing unprecedented potential in (mechano)biology and biomaterials. Arrays of pillar-like nanostructures, e.g., nanopillars, nanotubes, nanowires, with specific geometries and mechanical characteristics have been shown to influence the attachment, proliferation, and differentiation of mammalian cells [8,9] as well as inhibit

bacterial growth on the surfaces of implants [9–15].

The accurate characterization of the mechanical properties of individual nanopillars is a highly challenging yet fundamental aspect in the manufacturing and optimization of patterned surfaces. Indeed, the mechanical characteristics of the individual nanopillars vary depending on the material, geometry, and fabrication method and are fundamental in several applications. For example, the stiffness of the nanofeatures present on antibacterial surfaces determines their ability to penetrate and damage the bacterial cell wall, thereby affecting their killing efficiency [10,12,15]. Furthermore, it has been demonstrated that the differentiation of stem cells depends on the stiffness of the surface on which they grow [16–18]. As another example, arrays of compliant

* Corresponding author at: Department of Precision and Microsystems Engineering, Faculty of Mechanical, Maritime, and Materials Engineering, Delft University of Technology, Mekelweg 2, Delft 2628CD, The Netherlands.

** Corresponding author.

E-mail addresses: L.Angeloni@tudelft.nl (L. Angeloni), M.K.Ghatkesar@tudelft.nl (M.K. Ghatkesar).

¹ Equal contribution.

micropillars have been used to study the forces exerted by individual cells on surfaces [19,20]. The accuracy of the force measurements in these systems is strongly related to the accuracy of the estimation of the pillars stiffness.

The possibilities to measure the mechanical properties of single nanopillars are still severely limited by the lack of tools and methodologies that are easy to access and use. The existing techniques though efficient have certain limitations. They require mechanical testing tools to be mounted inside scanning electron microscopes (SEM). For instance, tensile [21–30], compression [31–34] and bending [34–38] tests have been performed on different kinds of micro- and nanopillars through the use of nanomanipulators, tensile machines, nanoindenters, or AFMs mounted inside SEM. In these cases, the use of SEM is necessary to position the punch or the tip on the nanostructure and to monitor its displacement in real-time during the application of the force. These instruments are expensive, difficult to use, and not available in all laboratories.

Another limitation is related to the sample characteristics. If the mechanical test has to be performed in an SEM chamber, samples need to be conductive. Therefore non-conductive samples have to be coated with metallic films influencing their actual mechanical properties. Furthermore, in many cases, the nanostructures need to be fixed to the testing machines [23–26]. Otherwise, samples with specific shapes (e.g., dogbone specimens) need to be fabricated [27,29]. This means that those techniques cannot be applied to nanopillars patterned on specific substrates.

Finally, SEM microscopy cannot be used if the measurements need to be performed under wet conditions, as is the case of (mechano)biological studies involving live cells in which the properties of the nanostructures may be affected by the presence of water.

To our knowledge, there are very few reports on AFM-based methods applied to the mechanical characterization of high aspect ratio nanostructures without SEM support. These tests consists in three- and two-points bending tests on double-anchored [39–46] or cantilevered [47] nanostructures, but cannot be applied to vertical pillar-like structures.

In this work, we present two AFM-based methods to perform mechanical tests on individual nanopillars and characterize their properties, without making use of SEM and without any sample modifications. These methods are based on two modes of operation that are available in most AFM equipment, *i.e.* contact mode imaging (CMI) and force spectroscopy imaging (FSI). Both techniques can be applied to micro- and nanopillars made with any aspect ratio, from any material, and on any substrate.

First, we present the working principles of both proposed methods, and the derivation of the equations needed to retrieve the mechanical parameters from experimental data. The methods are then used to characterize pillars produced by two-photon polymerization (2PP) and electron beam induced deposition (EBID). In the case of 2PP pillars, a complete mechanical characterization (*i.e.*, determination of the stiffness, maximum lateral force, maximum displacement, and maximum stress) was performed using both methods. In the case of conical EBID pillars, both proposed techniques were used to determine the maximum stress.

2. Materials and methods

2.1. Samples fabrication

2.1.1. 2PP polymeric pillars

Arrays of pillars with a diameter of 255 nm and a height of 500 nm, with 2.0 μm interspace between pillars and 10 μm interspace between lines were printed over an area of 500 μm x 500 μm by 2PP using a Photonic Professional GT equipment (Nanoscribe, Germany) as described elsewhere [11]. The pillars were printed in Galvo writing mode using the IP-L780 resin (Nanoscribe, Germany), a laser power of 14%, and a writing speed of 1200 $\mu\text{m}/\text{s}$. The samples were developed for 25 min in propylene

glycol monomethyl ether acetate (PGMEA, Sigma-Aldrich, Germany), cleaned 5 min in isopropyl alcohol (IPA, Sigma-Aldrich, Germany) and blow-dried with air. For the Young's modulus measurements, a disc-shaped sample of the IP-L780 resin with a diameter of 1.0 μm and a height of 500 nm was printed using the same parameters.

2.1.2. EBID nanopillars

A Helios Nano Lab 650 (FEI company, US) equipped for electron beam induced deposition was used to fabricate the Pt-C nanopillars. Trimethyl(methylcyclopentadienyl)-platinum (IV) (($\text{CH}_3\text{C}_5\text{H}_4$)Pt(CH_3)₃) was used as the precursor gas. An acceleration voltage of 17.8 kV and a beam current of 0.4 nA at a working distance of 4 mm were used. Using MATLAB (MathWorks, US) stream files, cone-shaped nanopillars with base diameter of 60 nm, height of 260 nm, and interspace of 340 nm, over a total area of 10 μm x 10 μm , were deposited on a silicon wafer. For the Young's modulus measurements, a disc-shaped sample with a diameter of 1500 nm and a height of 190 nm of the same material was prepared using the same deposition parameters.

2.2. SEM imaging

The morphology of the pillars was characterized by SEM using a dual beam Helios G4 CX FIB/SEM (FEI, Hillsborough, USA).

2.3. AFM experiments

2.3.1. To determine Young's modulus measurement of the nanopillars material

The measurements of the Young's modulus of the pillars' materials (IP-L780 and Pt-C) were performed in the quantitative imaging (QI) mode on the disc-shaped samples, using a JPK Nanowizard 4 instrument (Germany). Data were analyzed by using the JPK SPM data processing software (JPK instruments, v6.1, Berlin, Germany).

The Hertz model for a paraboloid probe was used to fit the force-distance curves and retrieve the elastic modulus of the samples:

$$F = k_{c,z} d_{c,z} = \frac{4}{3} \frac{E}{1-\nu^2} R_{tip}^{\frac{1}{2}} \delta^{\frac{3}{2}} \quad (1)$$

where $d_{c,z}$ is the deflection of the cantilever, $k_{c,z}$ the bending stiffness of the cantilever, E the elastic modulus of the sample, ν the Poisson ratio of the sample, R_{tip} the tip radius and δ the indentation depth. The elastic modulus of the sample E is proportional to the ratio $k_{c,z}/(R_{tip})^{1/2}$.

A diamond-coated probe (NM-TC, Bruker, Billerica, USA) with a nominal spring constant of 350 N/m was used. This probe was calibrated by a combination of the contact method (to determine the deflection sensitivity, S_z) and the relative method.

The relative method uses a reference sample to force the ratio $k_{c,z}/(R_{tip})^{1/2}$ to be the "correct" one at a certain indentation depth [48]. An arbitrary value of cantilever stiffness (the nominal value 350 N/m) was set and the value of tip radius to obtain the correct ratio $k_{c,z}/(R_{tip})^{1/2}$ was determined using reference samples with known elastic modulus, similar to the expected elastic modulus of the unknown samples. The reference material was scanned first, and the tip radius (R_{tip}) was adjusted to make the measured elastic modulus of the reference sample equal to its nominal value at a certain indentation depth. The measurements on the unknown sample were then performed with the same indentation depth used on the reference sample.

For IP-L780 characterization, the deflection sensitivity of the used cantilever was calibrated on a sapphire surface using the contact method and resulted in a value of $S_z = 21.33$ nm/V. A polystyrene sample with a nominal Young's modulus of 3 GPa was used as reference material and an indentation depth of 10 nm was set. A Poisson's ratio of 0.34 for the reference material (polystyrene) and 0.4 for IP-L780 was considered. The value of R_{tip} retrieved from calibration and used for the measurement on IP-L780 sample was 10 nm.

For Pt-C characterization, the deflection sensitivity of the used cantilever was calibrated on a sapphire surface using the contact method and resulted in a value of $S_z = 25.3$ nm/V. A fused-silica specimen with a nominal elastic modulus of 72 GPa (test samples kit, Bruker, Billerica, USA) was chosen as reference material and an indentation depth of 5 nm was used. A Poisson's ratio of 0.15 for fused silica and 0.3 for Pt-C was considered. The value of R_{tip} retrieved from calibration and used for the measurement on Pt-C sample was 90 nm.

The Hertz's contact mechanics model was used to calculate the Young's modulus from the force-distance curves recorded at each point of the scanned area.

2.3.2. To determine the mechanical characteristics of single nanopillars by CMI and FSI

For the mechanical tests on single nanopillars, contact mode and QI mode were used. A SSRM-DIA probe (Bruker, Billerica, USA) was used, with a cantilever length of 225 μm , a width of 50 μm , a thickness of 5 μm , a nominal spring constant of 27 N/m. The tip of the probe consists in a diamond square pyramid with a height (h_{tip}) of 5.57 μm , a length and a width (l_{tip} and $w/2$) of 5 μm (measured by SEM, as reported in [Supplementary Information](#)). Calibration (determination of sensitivity S_z and stiffness constant $k_{c,z}$) of the probes used for the mechanical tests of single pillars was performed by the thermal tune method.

3. CMI and FSI methods for the mechanical characterization of nanopillars

Contact mode (CMI) and force spectroscopy imaging (FSI) are well established AFM techniques. CMI is widely used to characterize the morphology of surfaces at the nanoscale [49]. FSI techniques, e.g., Force Volume (FV) available on Bruker systems and Quantitative Imaging (QI) available on Bruker JPK systems, are generally applied to perform nano-indentations of a specimen and have been extensively used for the measurement of the elastic modulus of both hard and soft materials [11, 51,52,62], as well as for the characterization of biological matter [52–55].

Here, we propose a new application for these techniques which consists of performing mechanical tests on single nanopillars to measure their elastic properties and failure strength, as sketched in Fig. 1a and c.

In the procedures we propose, the nanopillars of interest are scanned several times in CMI (in case of CMI method) or FSI (in case of FSI method), with increasing values of the setpoint force, i.e., gradually increasing the value of the force applied to the pillars, until they fracture. The failure of the pillar, in most cases, is visible in the topographies acquired with those high values of applied force. It can also be confirmed by acquiring an additional CMI or FSI topography image using a low non-destructive setpoint force.

To perform the mechanical tests on nanopillars by CMI or FSI, the first contact between the probe tip and the pillar must occur at the apex of the pillar. To satisfy this condition, the geometry of the probe, its mechanical properties, and the scan directions must be appropriately selected. Especially: i) the inclination angle between the sidewall of the pyramidal tip and its vertical axis must be greater than the inclination angle between the wall of the pillar and its vertical axis; ii) since, in most AFM equipment, the cantilever is tilted with respect to the horizontal plane, the contact between the tip and the pillar must occur on one of the front sidewalls of the AFM tip. If the contact occurs on the back sidewalls of the AFM tip, the first contact between the tip and the pillar could occur not at the apex of the pillar, but at the base; iii) the inclination angle of the facet of the AFM tip may not change during the experiments. This means that the rotation of the tip due to the possible torsion of the cantilever or bending of the tip must be negligible. Since most of commercial cantilevers have very high torsional stiffness (order of 10^3 N/m) as compared to the (bending) stiffness of micro and nanopillars samples, the rotation of the tip due to the cantilever torsion can be considered negligible. To obtain the negligible deformation (bending) of the tip, the

tip must be rigid. This means that short and large tips, made of hard material (e.g., diamond, such as the probe used in our work) are preferred.

Furthermore, since, in CMI, each line is scanned twice (trace and retrace), to avoid the contact from occurring on the back sidewalls of the AFM tip during one of the two scans, the AFM tip must scan the sample laterally, i.e., the fast scan direction must be set perpendicular to the long axis of the cantilever.

In these conditions, knowing the geometry of the probe, from the setpoint force and the measured signals in CMI or FSI, several mechanical parameters of the nanopillars can be determined. More specifically, both CMI and FSI methods allows for the quantification of:

- 171) The magnitude of the force applied to the pillar.
- 172) The displacement of the apex of the pillar at each level of the applied force.
- 173) The stiffness of the pillar.
- 174) The failure force and the maximum displacement of the pillar.
- 175) The height of the most stressed section.
- 176) Furthermore, if the geometry of the analyzed pillars is known, analytical equations or FEM simulations can be applied to estimate the maximum stress at the section at which the failure occurs.

Only in some specific circumstances (specified later) that generally depend on the geometry of the pillars and the probe, some of the parameters (e.g., the maximum displacement) cannot be determined.

3.1. CMI method

The tip positions and the corresponding photodiode signals during a CMI scan across the pillar are sketched in Fig. 1a.

The measured height, the vertical deflection error and the lateral deflection vary along the pillar cross section with the trends showed in Fig. 1b-1, b-2 and b-3 because of the interaction force between the (front) sidewalls of the AFM tip and the apex of the pillar. The maximum values of the vertical deflection error $\Delta V_{d_{err}}$ and the lateral deflection $\Delta V_{lat_{def}}$ (point C in Fig. 1a and b), have to be considered to calculate the maximum force applied to the nanopillar, as explained below.

When the pillar experiences significant deformation due to the lateral force applied by the AFM probe, the signal profiles cannot be symmetric (Fig. 1b-1). The distance Δx between the point of first tip-pillar contact (point B of Fig. 1a and b) and the point corresponding to the apex of the pillar (point D of Fig. 1a and b), can be used to determine the value of the displacement of the apex of the pillar, as explained below.

3.1.1. Calculation of the force applied to the pillar

Let us consider the cantilever geometry and the reference axes X, Y, Z (Fig. 2a–d).

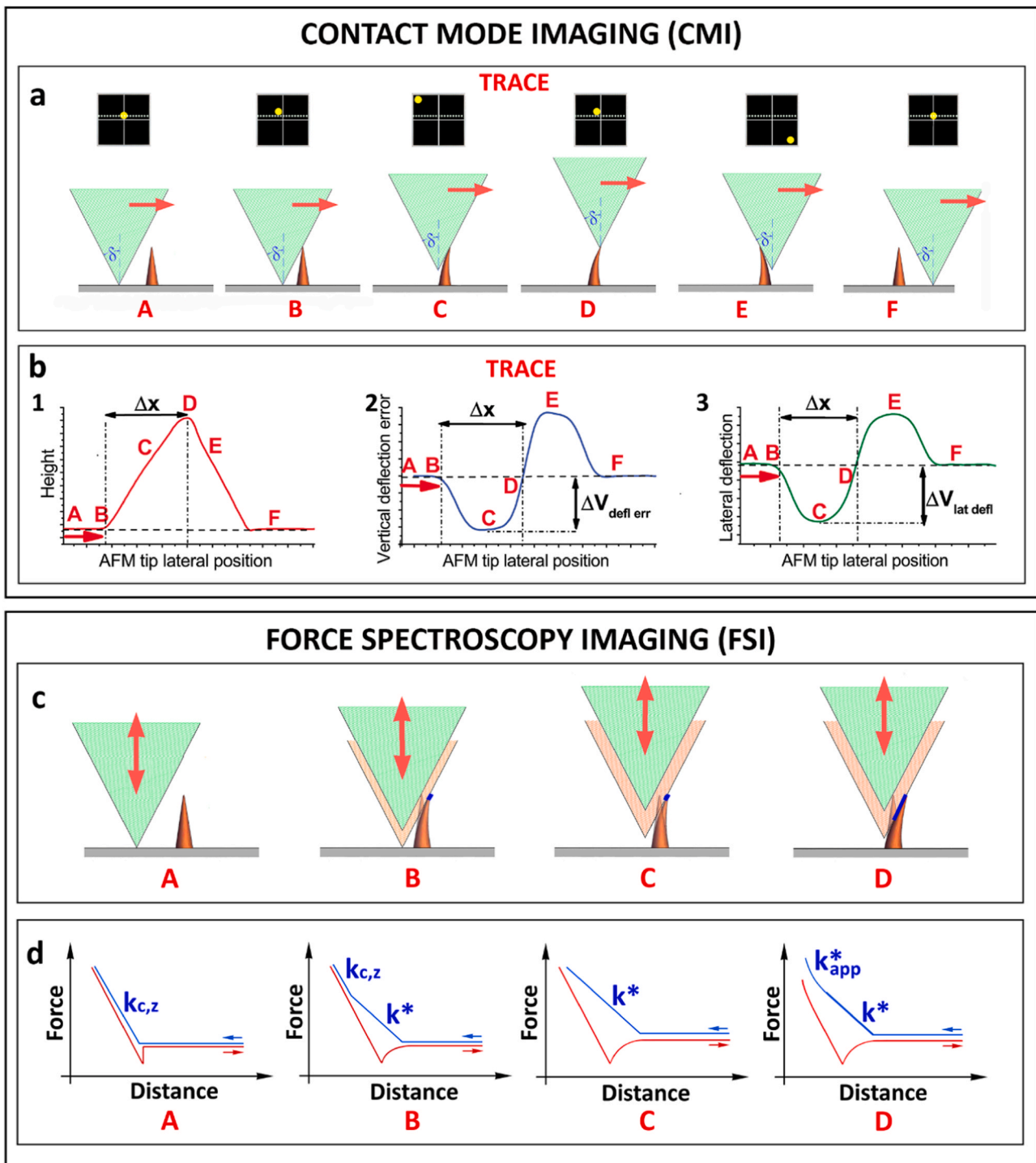
X and Y (Fig. 2a and c) are the fast and slow scan directions, respectively. The contact between the probe and the pillar occurs on one of the facets on the front of the pyramidal AFM tip (point C in in Fig. 2a). The force F_N applied to the pillar, is, therefore, directed along the normal to the plane of the face of the tip (Fig. 2a, d). F_N can be expressed in terms of its components along the directions X, Y, and Z as:

$$F_{N,x} = F_{N,xy} \cos \beta = F_N \cos \beta \cos \gamma \quad (2)$$

$$F_{N,y} = F_{N,xy} \sin \beta = F_N \sin \beta \cos \gamma \quad (3)$$

$$F_{N,z} = F_N \sin \gamma \quad (4)$$

where β is the half front angle of the base of the pyramidal AFM tip (Fig. 2c) and γ is the angle of the inclination of the wall of the tip relative to its vertical axis (Fig. 2d), which can be calculated as:



(caption on next page)

Fig. 1. Schematic drawings of the contact mode imaging (CMI) (a-b) and force spectroscopy imaging (FSI) (c-d) methods we propose for determining the mechanical characteristics of a nanopillar. a) Time sequence during a single CMI scan across a pillar (red cone) with a cantilever tip (green inverted pyramid) whose position is monitored by reflected laser light (yellow dot) on a four-quadrant photodiode (black square). (a-A) To begin, the cantilever tip, in contact with the substrate, is far away from the pillar; (a-B) the tip touches the pillar with its sidewall; (a-C) it goes upwards; (a-D) reaches the pillar apex; (a-E) goes downwards; (a-F) reaches the substrate. The angle δ is the half-cone angle of the AFM tip as seen from the front view. b) Representative profiles of the signals recorded during the contact mode scan: (b-1) pillar height, (b-2) cantilever vertical deflection error, and (b-3) cantilever lateral deflection. The signs of vertical deflection error and lateral deflection signals are just a convention: negative values correspond to the upward bending of the cantilever, while positive values correspond to the downward bending of the cantilever, as it is conventionally set in most AFM apparatus. The points A, B, C, D, E, and F indicate the signal value corresponding to the scan points sketched in Figures a-A, a-B, a-C, a-D, a-E, and a-F, respectively. Δx is the distance between the point of the first contact between the AFM tip and the pillar and the apex of the pillar. $\Delta V_{def\ err}$ and $\Delta V_{lat\ defl}$ are the maximum values of vertical deflection and lateral deflection signals, respectively. c) Time sequence during a single FSI scan across a pillar (red cone) with the cantilever tip (green inverted pyramid) that is moving vertically (shown as red double arrow). The green and red inverted pyramids represent different positions during the vertical movement. (c-A) Initially, the cantilever tip is far from the pillar and touches only the substrate. (c-B) the cantilever tip touches the pillar apex (blue dot) with its sidewall and continues downwards to touch the substrate. (c-C) the cantilever tip touches the pillar apex (blue dot) with its sidewall and continues downwards but does not reach the substrate. (c-D) the cantilever tip touches the pillar apex, continues downwards sliding along the pillar (blue line), and does not reach the substrate. Here, the pillar experiences high deformation and/or the inclination angle of the AFM tip is small (the pillar rotation is higher than the inclination angle of the AFM tip). d) The approach (blue) and retract (red) curves of the cantilever corresponding to each position illustrated in c). From the slope of the approach curve, the equivalent spring constant can be obtained. $k_{c,z}$ is the spring constant of the cantilever, k^* is the spring constant of the system “cantilever+pillar” (when the cantilever tip touches the nanopillar), and k^*_{app} is the apparent spring constant when the cantilever tip slides along the pillar. (For interpretation of the references to color in this figure legend, the reader is referred to the web version of this article.)

$$\gamma = \arctan\left(\frac{\overline{AB}}{h_{tip}}\right) = \arctan\left(\frac{l_{tip}\sin\beta}{h_{tip}}\right) \quad (5)$$

where h_{tip} is the height and l_{tip} is the length of the tip, respectively (Fig. 2b). The length of the segment \overline{AB} (Fig. 2c and d) is given by:

$$\overline{AB} = \frac{w}{2} \cos\beta = l_{tip}\tan\beta\cos\beta = l_{tip}\sin\beta \quad (6)$$

The lateral force $F_{N,xy}$ acting to the pillar, and producing the breakage, is, therefore, a force in the XY plane and equals the vector sum of the components $F_{N,x}$ and $F_{N,y}$, having the magnitude:

$$F_{N,xy} = \sqrt{F_{N,x}^2 + F_{N,y}^2} = F_N \cos\gamma \quad (7)$$

The value of the applied force F_N can be determined either from the measured total vertical deflection signal or from the measured lateral deflection signal, as explained below.

3.1.1.1. Calculation of the applied force from the total vertical deflection signal. When interacting with the pillar, the AFM cantilever can be described as a beam subjected to the combined action of a point load $P = F_{N,z}$ at its free end and a bending moment $M = -F_{N,y}(h_{tip} + t/2)$, where $t/2$ is the half-thickness of the cantilever (Fig. S1 of the Supplementary Information). Therefore, from the Euler-Bernoulli beam theory, the displacement $d_{c,z}$ of the free end of the cantilever can be calculated as:

$$d_{c,z} = \frac{PL^3}{3EI} + \frac{ML^2}{2EI} = \frac{1}{k_{c,z}} \left(F_{N,z} - \frac{3}{2} F_{N,y} \frac{(h_{tip} + \frac{t}{2} - h_{pillar})}{L} \right) \quad (8)$$

where E is the Young's modulus of the material, L is the length of the beam, I is the area moment of inertia of the cross-section, and $k_{c,z} = \frac{3EI}{L^3}$ is the stiffness constant of the AFM cantilever (assuming a rectangular cantilever beam with a uniform cross-section with the load applied at its free end and experiencing small deflections). $d_{c,z}$ is the measured total vertical deflection of the cantilever, given by the sum of the user-defined setpoint deflection ($d_{setpoint}$) and the deflection error (d_{err}).

Substituting $F_{N,z}$ and $F_{N,y}$ with Eqs. (3) and (4), Eq. (8) can be used to calculate the force F_N applied to the pillar as:

$$F_N = \frac{k_{c,z}d_z}{\sin\gamma - \frac{3}{2} \frac{(h_{tip} + \frac{t}{2} - h_{pillar})}{L} \sin\beta\cos\gamma} = \frac{k_{c,z}(d_{setpoint} + d_{err})}{\sin\gamma - \frac{3}{2} \frac{(h_{tip} + \frac{t}{2} - h_{pillar})}{L} \sin\beta\cos\gamma} \quad (9)$$

$$= \frac{k_{c,z}S_z(V_{setpoint} + \Delta V_{defl\ err})}{\sin\gamma - \frac{3}{2} \frac{(h_{tip} + \frac{t}{2} - h_{pillar})}{L} \sin\beta\cos\gamma}$$

where S_z is the vertical sensitivity, $V_{setpoint}$ is the setpoint photodetector signal and $\Delta V_{defl\ err}$ is the vertical deflection error signal, that can be measured from the deflection error profile (Fig. 1b-2). $k_{c,z}$ and S_z are usually measured before each AFM experiments using well-established protocols [56,57].

Since the height of AFM tips is generally in the range of 5–15 μm , if h_{pillar} is in the nano range, it can be often neglected and Eq. (9) can be rewritten as:

$$F_N = \frac{k_{c,z}d_z}{\sin\gamma - \frac{3}{2} \frac{(h_{tip} + \frac{t}{2})}{L} \sin\beta\cos\gamma} = \frac{k_{c,z}(d_{setpoint} + d_{err})}{\sin\gamma - \frac{3}{2} \frac{(h_{tip} + \frac{t}{2})}{L} \sin\beta\cos\gamma} \quad (10)$$

The components $F_{N,x}$, $F_{N,y}$, $F_{N,z}$, and $F_{N,xy}$ can be calculated from Eqs. (2), (3), (4), and (7), respectively.

3.1.1.2. Calculation of the applied force from the lateral deflection signal. Since the force F_N also has a lateral component $F_{N,x}$ (along the X-axis, Fig. 2c), acting at the end of the tip, the cantilever is also subjected to torsion and, therefore, experiences a lateral deflection. The X-component of the applied force, $F_{N,x}$, can then be estimated by:

$$F_{N,x} = k_{c,x}d_{c,x} = k_{c,x}S_x\Delta V_x \quad (11)$$

where $d_{c,x}$ is the measured lateral deflection that can be retrieved from the lateral deflection profile (Fig. 1b-3).

$k_{c,x}$ is the lateral stiffness of the cantilever-tip assembly with the lateral load applied at the end of the tip (torque), which can be calculated using the vertical stiffness $k_{c,z}$ (known from calibration) as [58]:

$$k_{c,x} = \frac{Gb^3}{3L(h_{tip} + \frac{t}{2})^2} = \frac{2}{3} \frac{L^2}{(h_{tip} + \frac{t}{2})^2} \frac{1}{(1+\nu)} k_{c,z} \quad (12)$$

where $G = \frac{E}{2(1+\nu)}$ is the shear modulus, b is the width of the cantilever, t is the thickness of the cantilever, and $\nu = 0.27$ is the Poisson ratio. S_x is the lateral sensitivity, which can be determined through the normal sensitivity S_z (known from calibration) via [58]:

$$S_x = \frac{E(h_{tip} + \frac{t}{2})}{2GL} S_z = \frac{h_{tip} + \frac{t}{2}}{\frac{L}{1+\nu}} S_z \quad (13)$$

assuming the photodiode to be rotationally symmetric. ΔV_x is the lateral signal measured by the photodiode.

Therefore, from Eq. (2), the force F_N applied to the pillar, can be also calculated as:

$$F_N = \frac{F_{N,x}}{\cos\beta\cos\gamma} = \frac{k_{c,x}S_x\Delta V_x}{\cos\beta\cos\gamma} \quad (14)$$

and the components $F_{N,y}$, $F_{N,z}$, and the lateral force $F_{N,xy}$ can be

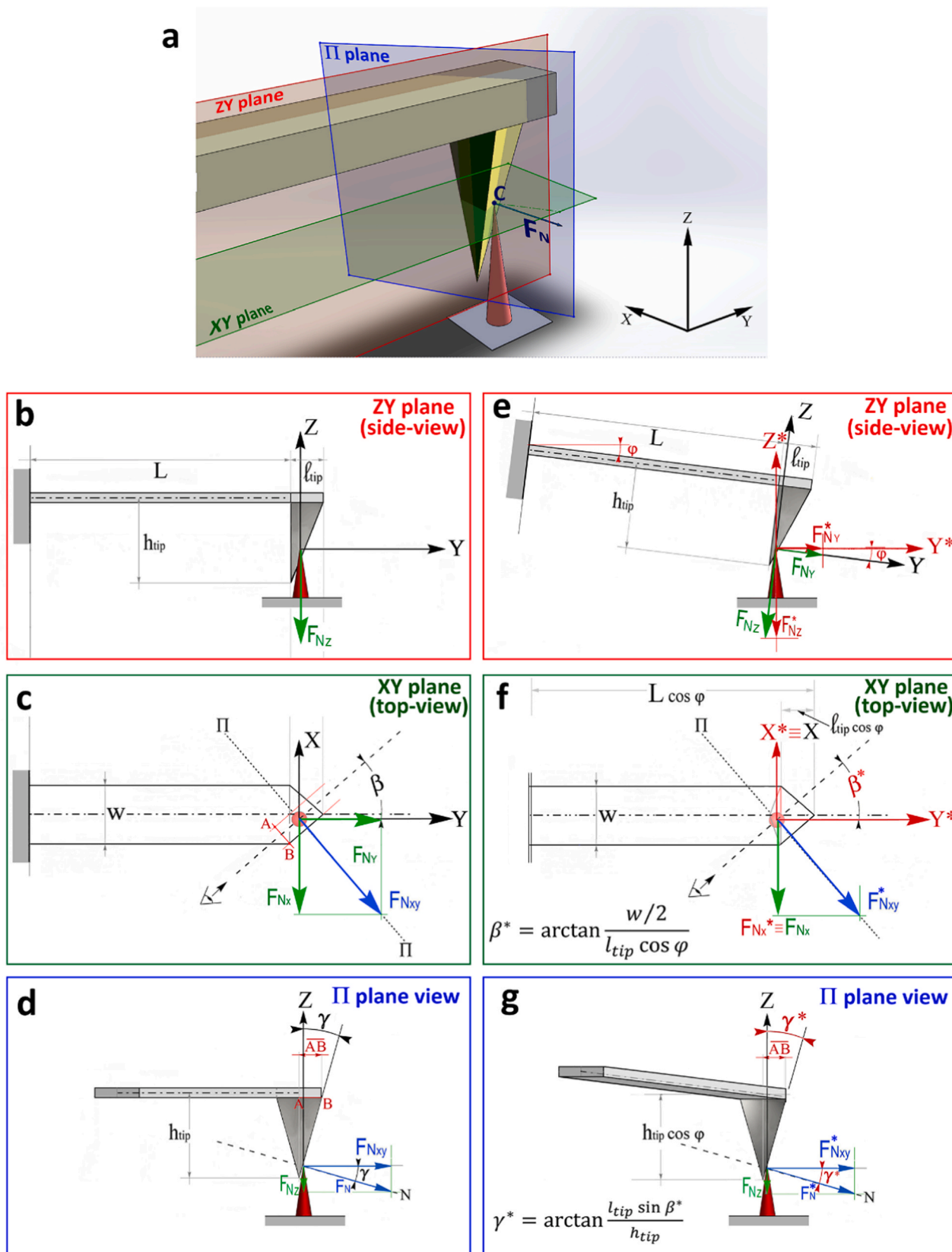


Fig. 2. Schematics drawings of the AFM probe geometry and the tip-pillar interaction force (F_N). a): 3D view of the AFM probe interacting with the pillar with the ZY (side-view), XY (top-view) and Π planes. Point C indicates the contact point with the pillar and the arrow indicates the direction of the tip-pillar interaction force (F_N). b-d): 2D views in the planes ZY, XY and Π of the AFM probe interacting with the pillar; e-g): 2D views when the cantilever is tilted by an angle φ , due to the tilting angle of the cantilever holder.

calculated from Eqs. (3), (4), and (7), respectively.

3.1.1.3. Correction for the tilt angle of the cantilever. In most AFM systems, the cantilever is tilted with an angle φ relative to the Y-axis to ensure that only the tip touches the sample surface. To take into account the tilting angle φ , we can consider a reference frame $X^* = X$, Y^* , Z^* jointed to the pillar (Fig. 2e-g).

In this case, the force F_N^* directed along the normal to the sidewall of the tilted tip can be calculated from the vertical deflection signal as:

$$F_N^* = \frac{k_{c,z}d_z}{\sin\gamma^* - \frac{3}{2}\frac{(h_{tip}+\frac{w}{2})}{L}\sin\beta^*\cos\gamma^*} = \frac{k_{c,z}(d_{setpoint} + d_{err})}{\sin\gamma^* - \frac{3}{2}\frac{(h_{tip}+\frac{w}{2})}{L}\sin\beta^*\cos\gamma^*} \quad (15)$$

and from the lateral deflection signal as:

$$F_N^* = \frac{F_{N,x}}{\cos\beta^*\cos\gamma^*} = \frac{k_{c,x}S_x\Delta V_x}{\cos\beta^*\cos\gamma^*} \quad (16)$$

where:

$$\beta^* = \arctan\frac{w/2}{l_{tip}\cos\varphi} \quad (17)$$

and

$$\gamma^* = \arctan\frac{l_{tip}\sin\beta^*}{h_{tip}} \quad (18)$$

The components of F_N^* along the directions $X^* = X$, Y^* and Z^* are:

$$F_{N,x}^* = F_N^*\cos\beta^*\cos\gamma^* \quad (19)$$

$$F_{N,y}^* = F_N^*\sin\beta^*\cos\gamma^* \quad (20)$$

$$F_{N,z}^* = F_N^*\sin\gamma^* \quad (21)$$

$$F_{N,xy}^* = F_N^*\cos\gamma^* \quad (22)$$

From now on, we will always refer to the values of forces and angles corrected for the cantilever tilt angle (i.e., F_N^* , $F_{N,x}^*$, $F_{N,y}^*$, $F_{N,z}^*$, $F_{N,xy}^*$, β^* , and γ^*). However, since the tilt angle of the cantilever is generally very small ($\varphi \leq 10^\circ$), in most cases it can be reasonably neglected. Indeed, if we consider the typical tilt angle of Bruker-JPK systems ($\varphi = 10^\circ$), and the geometry of a typical probe appropriate for this kind of measurements (e.g., SSRM-DIA from Bruker used in this work, having the following dimensions: $h_{tip} = 5.57 \mu\text{m}$, $w/2 = 5 \mu\text{m}$, and $l_{tip} = 5 \mu\text{m}$), the difference between β and β^* is $<1\%$ ($\beta = 45^\circ$ and $\beta^* = 45.438^\circ$) while the difference between γ and γ^* is 0.6% ($\gamma = 32.876^\circ$ and $\gamma^* = 33.075^\circ$). If the correction for the tilt angle is negligible, all the reported equations can be used without such a correction.

3.1.2. Calculation of the displacement and the stiffness of the pillar

The displacement of the center of the apex of the pillar occurring when a certain lateral force $F_{N,xy}^*$ is applied can be calculated as:

$$d_{pillar} = \frac{d_{pillar,x} - R_{pillar}}{\cos\beta^*} \quad (23)$$

where $d_{pillar,x}$ is the component of the displacement along the X direction and R_{pillar} is the half-width of the pillar (i.e., the radius in case of a circular section). Since the fast scan direction corresponds to the X direction, $d_{pillar,x}$ can be retrieved from the profile of the pillar in the CMI topography corresponding to the section where the maximum height (i.e., the apex) of the pillar is observed. Indeed, $d_{pillar,x}$ is:

$$d_{pillar,x} = \Delta x - \Delta x_{tip\ convolution} \quad (24)$$

where Δx is the distance (along the X direction) between the point of the first contact of the AFM tip with the pillar (B in Fig. 1a and b) and the point of the maximum height, (D in Fig. 1a and b). $\Delta x_{tip\ convolution}$ is the

convolution of the AFM probe:

$$\Delta x_{tip\ convolution} = h_{pillar}\tan\delta \quad (25)$$

where h_{pillar} is the height of the pillar and δ is:

$$\delta = \arctan\left(\frac{w/2}{h_{tip}\cos\varphi}\right) \quad (26)$$

where $w/2$ is the half-width of the AFM tip.

By plotting the obtained values of the lateral force $F_{N,xy}^*$, and lateral displacement d_{pillar} calculated for each setpoint value, the force-displacement curve for each analyzed pillar can be obtained. If a linear trend is observed, the slope of the force-displacement curve is the value of the stiffness of the pillar, which can be also used to estimate the maximum displacement of the pillar.

Indeed, when the rupture force $F_{N,xy,max}^*$ is applied, the pillar breaks and it is not possible to retrieve the maximum displacement from the topography at that force. However, knowing the stiffness of the pillar from the force-displacement curve, the maximum displacement of the pillar $d_{pillar,max}$ can be estimated as:

$$d_{pillar,max} = \frac{1}{k_{pillar}}F_{N,xy,max}^* \quad (27)$$

3.2. FSI method

In FSI, a force-distance (F-d) curve is acquired at each point of the scanned area.

In Fig. 1c-d, a schematic of the working principle of the proposed FSI mode method is shown. Fig. 1c shows the sketches of the positions of the tip relative to the pillar during the scan of a cross section of the pillar. In Fig. 1d, the corresponding representative force-distance curves are shown.

At the scan points far away from the pillar, the tip interacts only with the substrate (Fig. 1c-A). The corresponding F-d curve is shown in Fig. 1d-A. It is worth reminding that an AFM probe in contact with the sample can be modeled as a series of two springs, $k_{c,z}$, and k_{sample} , representing the stiffness of the cantilever and the sample, respectively. Therefore, the equivalent stiffness k^* of the system cantilever + sample is:

$$k^* = \frac{k_{c,z}k_{sample}}{k_{c,z} + k_{sample}} \quad (28)$$

If the substrate is rigid, no indentation occurs and the contact region of the approach curve has a linear trend, the slope of which is the spring constant of the cantilever $k_{c,z}$:

$$\frac{1}{k^*} = \frac{1}{k_{c,z}} + \frac{1}{k_{sample} \rightarrow \infty} = \frac{1}{k_{c,z}} \quad (29)$$

As the scanning continues across the nanopillar, at some points the sidewall of the tip comes in contact with the apex of the pillar first and continues to move towards the substrate until the defined setpoint force value is reached (Fig. 1c-B). At these points, the contact region of the approach curve appears as two distinct segments with two different slopes (Fig. 1d-B). The slope of the first region of the curve, where the sidewall of the tip is in contact with the apex of the pillar without touching the substrate, is k^* :

$$\frac{1}{k^*} = \frac{1}{k_{c,z}} + \frac{1}{k_{pillar}} \quad (30)$$

assuming a point contact between the probe and the pillar. The slope of the second region, where the apex of the AFM probe is in contact with the substrate, is the stiffness of the cantilever $k_{c,z}$.

When the AFM tip moves closer to the pillar (Fig. 1c-C), the F-d curve is similar to the one shown in Fig. 1d-C. During the approach, the sidewall of the AFM probe comes into contact with the pillar, the tip

descends till the setpoint force value is reached. The apex of the AFM probe does not reach the substrate in this case. If the contact between the tip and the pillar is a point contact occurring at the apex of the pillar, as sketched in Fig. 1c-C, and the pillar is in the elastic regime, the trend of the contact region of the approach curve is linear and its slope equals the stiffness k^* of the system “cantilever + pillar” (Eq. 30). These curves correspond to the scan points where the tip applies maximum force to the pillar. Such curves are used for the calculation of the mechanical properties of the pillars.

In some cases, when a sharp probe is used and/or the pillar experiences significant deformation during the experiments, the rotation of the pillar can reach the value of γ^* (i.e., the inclination angle of the facet of the tip). In such cases, during the approach, the facet of the tip rests against the pillar and “glides” along its sidewall (Fig. 1c-D). This case, in which an apparent increase of the stiffness of the system “cantilever+pillar” (k^*_{app}) is observed, will be analyzed in more detail in the paragraph 3.2.2.

As the scanning continues, the apex of the AFM probe comes into contact with the apex of the pillar and then overcomes it. The contact occurs on the other front sidewall of the tip and the same type of curves will be obtained on the other side of the pillar.

3.2.1. Calculation of the mechanical parameters of the pillar: case of linear force-distance curve

Similar to the CMI method, the force F^*_N applied to the nanopillar, is directed along the normal to the plane of the sidewall of the tip where the contact with the apex of the pillar occurs. The force components are given by Eqs. (19)–(22).

Assuming the contact between the sidewall of the AFM tip and the pillar as a point contact (Fig. 1c-C) and the pillar in the elastic regime, the magnitude of the force F^*_N (applied to the apex of the pillar) can be calculated from the Euler-Bernoulli beam theory as:

$$F^*_N = \frac{k^* d_{c,z}}{\sin\gamma^* - \frac{3}{2} \frac{(h_{tip} + \frac{L}{2} - h_{pillar})}{L}} \sin\beta^* \cos\gamma^* \quad (31)$$

where k^* is the “equivalent” spring constant of the system cantilever + pillar, which can be estimated as the slope of the contact region of the force-distance curve measured when the tip is in (point) contact with the pillar, and $d_{c,z}$ is the measured vertical deflection of the cantilever. In the case of pillars in the nanometer range, h_{pillar} can be neglected.

The stiffness of the pillar (k_{pillar}) is obtained from Eq. (30) and the corresponding displacement of the apex of the pillar can be estimated as $d_{pillar} = F^*_N / k_{pillar}$.

3.2.2. Calculation of the mechanical parameters of the pillar: case of “non-linear” force-distance curve

If the rotation of the pillar, due to the applied force, reaches the value γ^* (i.e., the inclination angle of the sidewall of the AFM tip), the AFM tip slides along its lateral wall (Fig. 1c-D). The resultant force F^*_N is, in this case, not applied to the apex of the pillar but is progressively applied to lower heights. This phenomenon is characterized as the “apparent” stiffening of the pillar. It can be recognized in the recorded force-distance curves, by a progressive increase of the equivalent stiffness constant of the system cantilever + pillar (Fig. 1d-D). The contact region of the approach curve, in this case, is divided into two distinct regions. At low levels of force, the contact between the probe and the pillar is a point contact and occurs at the apex of the pillar. The curve in this region is linear and its slope is $k^* = \frac{k_{c,z} k_{pillar}}{k_{c,z} + k_{pillar}}$, which can be used to retrieve the pillar stiffness. For high values of the force, starting from the point where the tip starts sliding along the pillar sidewall, the curve is not linear but is characterized by a progressive increase of its slope.

In this case, the force F^*_N applied to the pillar can be calculated as:

$$F^*_N = \frac{k^*_{app} d_{c,z}}{\sin\gamma^* - \frac{3}{2} \frac{(h_{tip} + \frac{L}{2} - h_{pillar})}{L}} \sin\beta^* \cos\gamma^* \quad (32)$$

where k^*_{app} is the “apparent” stiffness of the system, calculated as the slope of the force-distance curve in correspondence with the highest values of the applied force (Fig. 1d-D).

In this case, the calculated force F^*_N , should not be considered to be applied at the apex of the pillar for the calculation of other mechanical parameters, such as the maximum stress at the most loaded section. Instead, it should be considered applied at a lower height, which needs to be determined.

Different ways to calculate the height where the force is applied are possible. In general, analytical or numerical models can be used. In one of the case studies presented here on EBID conical nanopillars, we analytically calculated from the residual height of the pillar after its fracture.

It is worth noting that, also in case the pillar experiences plastic deformation the force-distance curve could have a non-linear trend. Also, in this case, the force should be calculated considering the value of k^*_{app} corresponding to the highest values of applied force.

4. Results and discussion

In this section, we report two cases studies where the CMI and FSI methods are applied for the mechanical characterization of nanopillars: i) 3D printed polymeric pillars produced by 2PP and ii) Pt/C nanopillars deposited by EBID.

4.1. Morphological analysis and measurement of elastic modulus of 2PP and EBID nanopillars

The 2PP 3D printed nanopillars were cylinders rounded at the tip with a base diameter of 250 nm (Fig. 3a) and a height, measured by AFM QI mode, of 529.7 ± 7.3 nm. EBID pillars exhibited a conical shape, with a base diameter of 60 nm and a height of 259.6 ± 2.4 nm (Fig. 3b).

The elastic modulus of the materials was measured in QI mode on disc-shaped samples of the same materials, deposited on the same substrates (glass for 2PP pillars and silicon for EBID pillars) using the same deposition parameters of the pillars. The IPL-780 disc-shaped structure had a diameter of 1.5 μ m and a height of 500 nm. The EBID disc-shaped structure had a diameter of 1 μ m and a height of 190 nm. It was 3.34 ± 0.6 GPa (Fig. 3c) for the IP-L780 resin used for 2PP pillars fabrication, in good agreement with the values provided by the supplier of the resin and with our previous results [11], and 17.8 ± 1.5 GPa (Fig. 3d) for Pt-C, in good agreement with previous results obtained on similar EBID structures [34,59].

4.2. 2PP nanopillars

4.2.1. Mechanical characterization using the CMI method

Mechanical characterization using the CMI method was conducted on 8 pillars. The pillars broke for a setpoint force ranging between 30 and 90 nN. An example of experiment on 2 nanopillars is reported in Fig. 4a-1-a-15.

After each scan in CMI, the possible changes in the morphology of the sample (e.g., the failure of the pillars) were evaluated by acquiring a topography image in the QI mode with a low setpoint force (10 nN) (Fig. 4a-4, a-9, a-14).

When a moderate setpoint force was set (30 nN in the example reported in Fig. 4), pillars remained intact (Fig. 4a-1-a-4). By increasing the setpoint force (to 50 nN in the example of Fig. 4), some of the pillars broke (Fig. 4a-6-a-9). The value of the setpoint force was then further increased (60 nN in the example of Fig. 4) and all the pillars failed (Fig. 4a-11-a-14).

The cross-sections profiles of the measured signals exhibited the

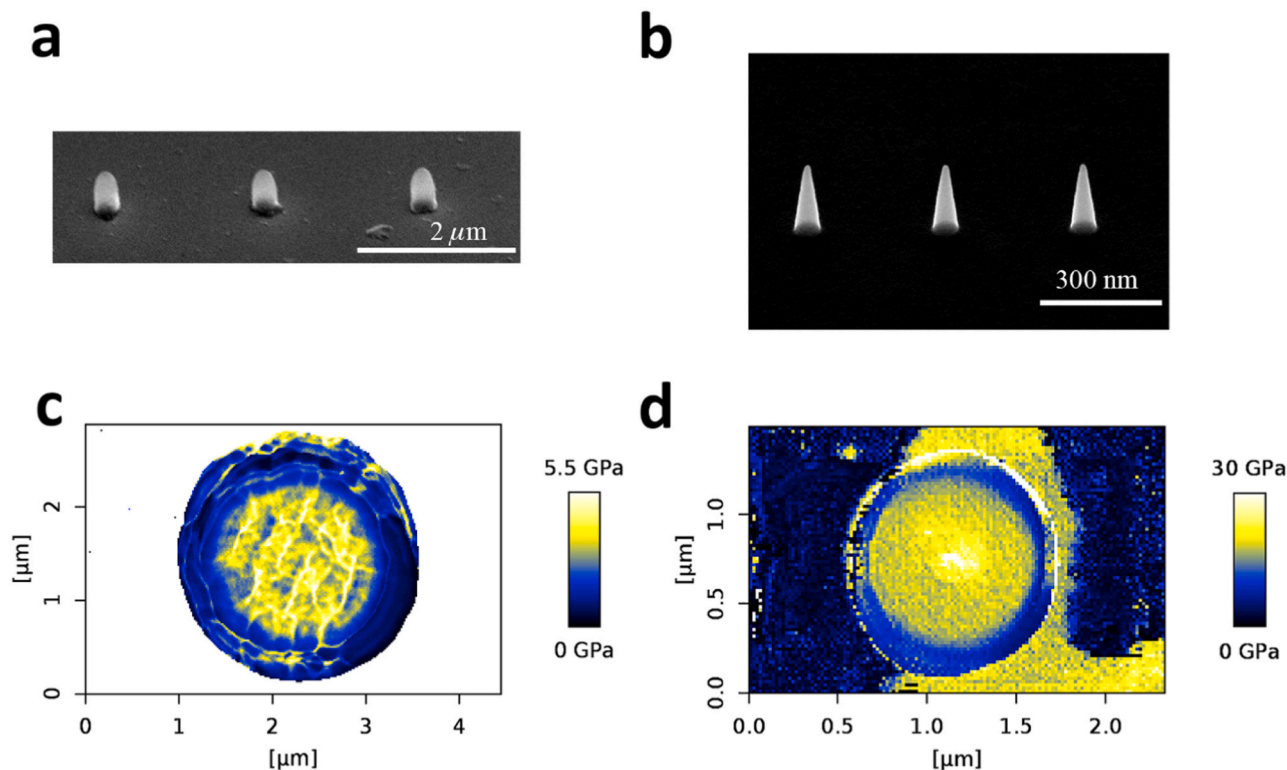


Fig. 3. SEM images of the (a) 2PP-printed pillars, (b) EBID-fabricated nanopillars. The elastic modulus of the materials used c) IP-L780 resin for 2PP printing and d) Pt/C for EBID were obtained by printing disc-shaped samples and performing AFM QI mode mapping across the specimens.

expected trends (previously shown in Fig. 1). An examples of height profile is shown in Fig. 4b-1. It was zero when the AFM tip was scanning the substrate (point A). It started to increase when the tip came into contact with the pillar (point B) and reached a maximum at the apex of the pillar (point D). Then, the height suddenly decreased when the tip overcame the apex and it came back to zero when the tip touched the substrate again (point F). All the measured contact mode height profiles appeared asymmetric (Fig. 4b-1), indicating a visible deformation of the pillar when subjected to the interaction force with the AFM probe.

A trend coherent to the height profile was observed for the vertical deflection error profile (Fig. 4b-2). An increase of the negative (upward) vertical deflection error was observed when the contact between the sidewall of the AFM tip and the apex of the pillar occurred (point B). The signal reached a maximum (C) and then came back to zero in the region corresponding to the apex of the pillar (point D). The inversion of the signal was then observed after the AFM tip overcame the apex of the pillar (point E).

A similar trend was observed for the lateral deflection profile (Fig. 4b-3). The signal rapidly increased when the probe-pillar contact occurred (B), and reached a maximum (C). When the apex of the AFM tip reached the apex region of the pillar (D), the lateral deflection was zero. After passing the apex of the pillar, lateral deflection signal inverted (point E), and came back to zero when the tip touched the substrate.

For each pillar, the values of applied force (F^*_{N}) and its lateral component $F^*_{N,xy}$ corresponding to each setpoint force were calculated from the lateral deflection signal, by applying Eqs. (16) and (22). The average value of the maximum lateral force $F^*_{N,xy,max}$ (i.e., the lateral component of the force corresponding to the setpoint force at which the rupture of the pillars was observed) resulted in 883.0 ± 89.5 nN.

The displacement of the apex of the pillar corresponding to each level of applied lateral force was calculated from the height profiles using Eqs. (23)–(26). The measured displacement values as a function of the corresponding applied lateral forces were plotted in Fig. 4c. The results show a linear trend ($R^2 > 0.97$ for all the curves), suggesting the

elastic behavior of the pillars under the entire range of applied forces. This was also confirmed by the topography images acquired in QI mode with low set point force (10 nN) after each level of applied force. Indeed, on those images, no changes in the pillar morphology (i.e., no displacements of the tips of the pillars) were observed even after the highest values of forces were applied. This indicates the absence of plastic deformation: the pillars elastically bent when the force was applied and came back to their initial position when the force was removed.

We calculated the stiffness of each pillar as the inverse slope, i.e., as the ratio $k_{pillar} = F^*_{N,xy}/d_{pillar}$. The calculated average value of stiffness for the analyzed pillars were 13.5 ± 3.2 N/m.

To validate our results, we compared the value of elastic modulus calculated from the value of stiffness of the pillars obtained by using our CMI method and the elastic modulus measured by a conventional, well established AFM technique: QI mode mechanical mapping.

Assuming pillars perfectly cylindrical, we calculated the corresponding value of elastic modulus as $E = \frac{k_{pillar} R_{pillar}^3}{3I}$, with $I = \frac{\pi R_{pillar}^4}{4}$ the area moment of inertia and R_{pillar} the radius of the circular section of the pillar. The elastic modulus corresponding to the experimental stiffness resulted in 3.23 ± 0.7 GPa. It is in very good agreement (only 3.3% lower) as compared to the value measured (3.34 ± 0.6 GPa) by conventional QI mode on the disc-shaped sample, indicating an accuracy of 3.3% of the CMI measurement. Furthermore, the precision of CMI method (coefficient of variation of 21%) resulted similar to the precision of conventional QI mode (coefficient of variation of 18%).

The consistency between the elastic modulus retrieved from the stiffness obtained by CMI method and the elastic modulus obtained by conventional QI mode indicates the correct estimation of the values of forces and displacements measured by CMI (Fig. S3). Indeed, in CMI, the stiffness is retrieved as the ratio between the estimated value of the applied force and the corresponding measured value of displacement ($k_{pillar} = F_{N,xy}/d_{pillar}$). Force and displacement are independently measured: the value of force was retrieved from the lateral displacement

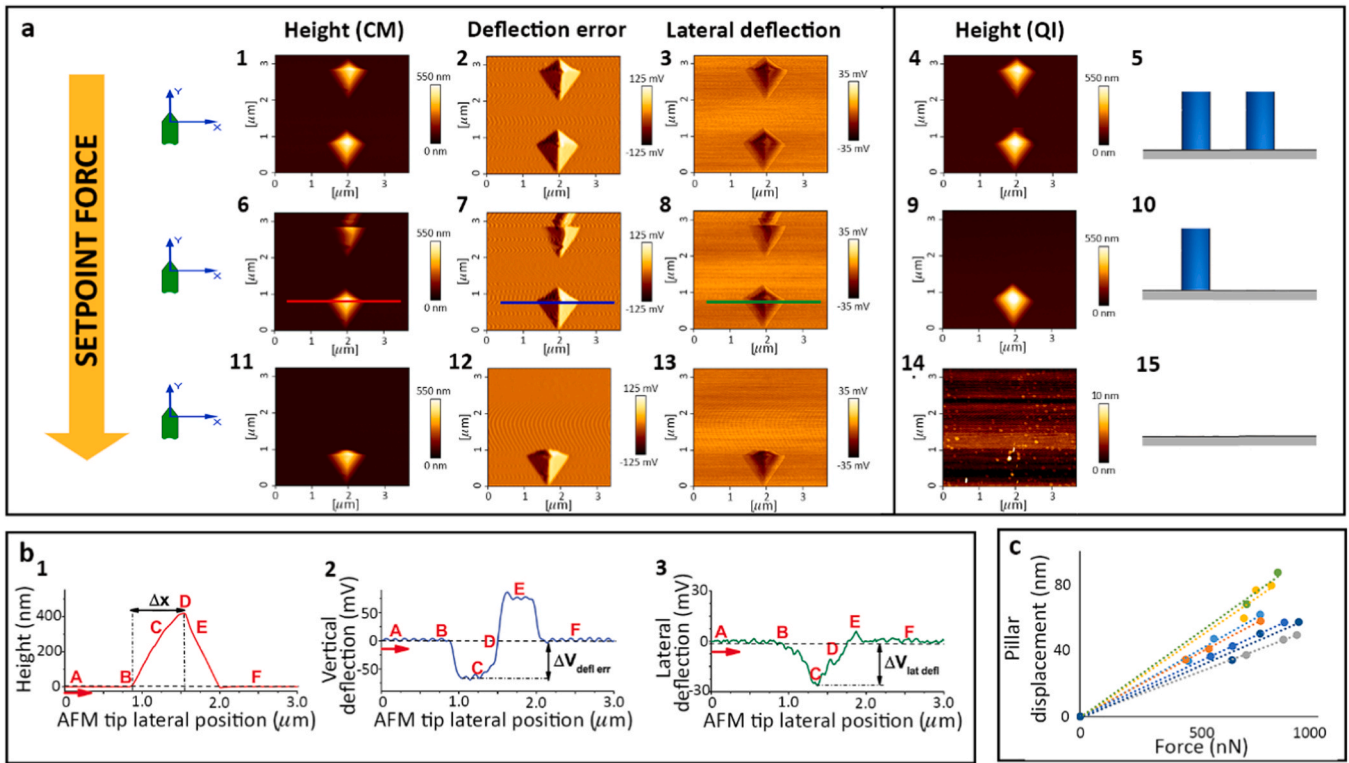


Fig. 4. Mechanical tests performed by using the CMI method on the 2PP 3D printed pillars. a) AFM images acquired during the tests: topography (a-1, a-6, a-11), deflection error (a-2, a-7, a-12) and lateral deflection (a-3, a-8, a-13) with increasing values of setpoint forces (30 nN, 50 nN, 60 nN). After the application of each setpoint force level, the morphology of the pillars was checked by acquiring topography images in QI mode with a lower setpoint force of 10 nN (a-4, a-9, a-14). The corresponding pillars morphology is sketched in a-5, a-10, a-15. b) Height (b-1), vertical deflection error (b-2) and lateral deflection (b-3) profiles corresponding to the sections of the pillar evidenced in figures a-6, a-7 and a-8, respectively. c) Summary of the experimental data ($F_{N,xy}^*$ and d_{pillar}) retrieved from the experiments and plotted in a force-displacement graph. The values of applied lateral force were determined by applying Eqs. (16) and (22), and the pillar displacement was obtained from Eq. (23). The data were fitted with linear curves ($R^2 > 0.97$ for all the curves). The inverse slope of the plot gives the pillar stiffness (k_{pillar}).

of the cantilever and the geometry parameters of the probe through Eqs. (16) and (22); the value of the displacement is retrieved from the measured topography data, through Eq. (23). Since the measurements of the two parameters are independent, the probability that there is a systematic and equal error on the two measurements performed on all the pillars can be considered almost null.

The maximum displacement of each pillar was estimated from experimental data as $d_{max} = F_{max}/k_{pillar}$ (last points in the curves reported in Fig. 4c). The average value of the maximum displacement was 64.2 ± 13.6 nm, corresponding to a rotation of 6.9° , significantly lower than the angle γ^* of the used probe (33.07°). This result suggests that the contact between the sidewall of the probe and the pillars is a point contact occurring at the apex of the pillar. Indeed, for cylindrical pillars, the sidewall of the tip can rest against the pillar only if the rotation of the tip reaches the value of the angle γ^* .

A further validation of the results was obtained by comparing our experimental data with theoretical values.

To validate the maximum displacement derived from the acquired experimental data, we analytically (from fundamental beam theory) calculated the deformation of the apex of the pillars subjected to a lateral force equal to the measured value of the rupture lateral force $F_{N,xy,max}^*$ at its apex as:

$$d_{pillar} = \frac{F_{N,xy,max}^* h_{pillar}^3}{3EI} = \frac{4}{3} \frac{F_{N,xy,max}^* h_{pillar}^3}{\pi R_{pillar}^3 E} \quad (33)$$

The elastic modulus of the material E was considered equal to the value measured by conventional QI mode measurement (3.34 GPa). An average value of the maximum lateral displacement of 68.2 ± 6.9 nm was obtained. This value is in good agreement (5.8% higher) with the

experimentally derived maximum displacement, confirming the consistency of the results obtained by our CMI method.

The topography images acquired in QI mode with low setpoint force (10 nN) after the breakage of the pillars, revealed the absence of any residue of the pillar showing a perfectly smooth surface (Fig. 4a-14). This result suggests that the failure of the studied pillars does not occur because of the fracture of the material, but because of their detachment from the substrate due to their poor adhesion. Indeed, if the polymeric material fractured, some residues should have been present on the substrate and visible in AFM images. This is in agreement with previous studies that revealed poor adhesion of similar structures deposited by the 2PP method [60], mainly due to the development step involved in the process. Nevertheless, to our knowledge, no measurements of the maximum stress and adhesion force of those structures to the substrates were conducted experimentally.

By using our experimental results and Euler-Bernoulli theory, it was possible to calculate the maximum stress, assumed as the maximum bending stress:

$$\sigma_{max} = \frac{MR}{I} = \frac{F_{N,xy}^* h_{pillar} R_{pillar}}{I} = 4 \frac{F_{N,xy}^* h_{pillar}}{\pi R_{pillar}^3} \quad (34)$$

where $M = F_{N,xy}^* h_{pillar}$ (with h_{pillar} , the height of the pillar) is the bending moment and A the area of the circular section of the pillar with radius R_{pillar} .

The maximum bending stress was found to be 0.3 ± 0.03 GPa. It is worth noting that we neglected the compression stress due to the vertical component of the applied force $F_{N,z}$ (0.01 GPa), being one order of magnitude lower than the bending stress, and the possible stress due to capillarity. We could retrieve the adhesion force of the pillar to the

substrate as $F_{adh} = \sigma_{max} A$. The adhesion force of the studied 2PP pillars was found to be $56.6 \pm 4.5 \mu\text{N}$.

In summary, the application of our CMI method to the mechanical characterization of the 2PP 3D printed pillars allowed us to successfully determine: i) the stiffness of the pillars, ii) the elastic modulus of the material (confirmed by the conventional QI mode), iii) the maximum lateral force (applied at the apex of the pillar), iv) the maximum displacement, from which it was possible to analytically estimate v) the maximum stress and, consequently vi) the adhesion force of the pillars to the substrate. The obtained quantitative results are summarized in Table 1 and are compared with the values obtained by FSI method, described in the following paragraph.

4.2.2. Mechanical characterization using the FSI method

Equivalent mechanical characterization of the same 2PP 3D printed polymeric pillars was conducted using the alternative FSI method (QI mode) and the results were compared and validated with the results obtained by the CMI method.

The range of setpoint forces in which the pillars were observed to break was 700–1200 nN, as shown in the representative example of Fig. 5a, where the QI topography images of a pillar acquired with increasing values of setpoint force are shown. When low values of setpoint forces were applied, no changes in the morphology of the pillar were observed (as sketched in Fig. 5a-5 and a-6). When higher values of setpoint forces were applied, the pillars broke (Fig. 5a-3) and no residues were found on the surface after failure (shown in the topography image of Fig. 5a-4 and sketched in Fig. 5a-7 and a-8).

Fig. 5b-1 shows a F-d curve acquired on the substrate (position sketched in Fig. 1c-A). The slope of the contact region (approach curve) on the rigid glass substrate gives the stiffness of the cantilever $k_{c,z}$ (13.3 N/m). Fig. 5b-2 shows a F-d curve acquired when the tip touches the pillar (position sketched in Fig. 1c-B). The contact region in the approach curve had two different segments: i) a region with lower slope, when the sidewall of the AFM tip touched the pillar (low values of force), whose value is the stiffness k^* of the system “cantilever +pillar” and ii) a region with higher slope, when the AFM tip apex went further and touched the rigid substrate, whose value is equal to the stiffness of the cantilever $k_{c,z}$.

In Fig. 5b-3, a F-d curve acquired with the tip touching only the pillar (position sketched in Fig. 1c-C) is shown. These curves were considered for the calculation of the mechanical parameters of the pillars. The contact region of the approach curve appeared linear. This indicated that a point tip-pillar contact occurred at the apex of the pillar for the entire range of applied force values and that the pillar bending was in the elastic regime. This confirms the analogous observation made in CMI method, where the maximum rotation of the apex of the pillars was significantly lower than the angle γ^* , indicating no resting of the AFM tip against the sidewall of the pillar. The stiffness of the pillars was estimated from the slope of these curve (three curves for each pillar were considered) using Eq. (30). The average value of the stiffness analyzed from 9 different pillars resulted in $15.9 \pm 2.6 \text{ N/m}$. This value is in good agreement compared to the value obtained by CMI method

($13.5 \pm 3.2 \text{ N/m}$), as the difference (17%) is in the same range of the experimental variability observed for the two methods. This value of stiffness corresponds to a value of elastic modulus of $3.8 \pm 0.6 \text{ GPa}$ (calculated assuming a cylindrical pillar), which is in good agreement with the values measured by conventional QI mode ($3.34 \pm 0.6 \text{ GPa}$), indicating an accuracy of 13.8% of the FSI measurement. The result was consistent with the result obtained by the CMI method ($3.23 \pm 0.77 \text{ GPa}$), the difference between the values being in the same range of the experimental variability. Furthermore, the precision of FSI method (17.7%) resulted similar to the precision of conventional QI mode (18%).

The applied force F_N^* and its lateral component $F_{N,xy}^*$ were estimated using Eqs. (31) and (22), where the value of k^* was retrieved as the slope of the entire contact region of the approach curves (average values of three curves for each pillar). The average value of the lateral rupture force of the analyzed pillars was $889.65 \pm 113.61 \text{ nN}$, in very good agreement with the value previously found by the CMI method.

The values of $F_{N,xy,max}^*$ and the stiffness k_{pillar} were reported in a force-displacement graph in Fig. 5c. k_{pillar} is the inverse slope of the reported curves. We estimated the maximum lateral displacement of the apex of the pillars using the experimental data as $d_{pillar,max} = F_{N,xy,max}^*/k_{pillar}$. An average value of $58.4 \pm 14.2 \text{ nm}$ was found, which was consistent with the values obtained with the CMI method (64.2 ± 13.6). To verify the result, we analytically calculated the maximum displacement of the pillar as the deformation of the apex of a cylindrical pillar subjected to the maximum lateral force $F_{N,xy,max}^*$ (i.e., using Eq. 33). It was done by considering the elastic modulus of the material equal to the value measured by conventional QI mode measurements (3.34 GPa). We found a value of $68.7 \pm 8.8 \text{ nm}$, in agreement with the values similarly calculated using the CMI data ($68.2 \pm 6.9 \text{ nm}$).

Topography images acquired in the QI mode with low setpoint force (10 nN) after the breakage of the pillars showed the absence of residues, confirming the complete detachment of the pillars from the substrate. The failure of these pillars was therefore confirmed to be due to the poor adhesion to the substrate and not to the fracture of the material, as already observed by using the CMI method.

From the experimental data obtained with the FSI method, the maximum stress of the pillar calculated as the maximum bending stress using Eq. (34) resulted to be $0.3 \pm 0.02 \text{ GPa}$. It is worth noting that we neglected the compression stress due to the vertical component of the applied force $F_{N,z}$ (0.01 GPa), being one order of magnitude lower than the bending stress. We also neglected the stress due to capillarity. Indeed, the adhesion force due to capillarity was found to be about 120 nN (Fig. 5b-3, peak of retract curve) which produces a local stress two orders of magnitude (about 0.003 GPa) smaller than the bending stress.

The adhesion force of the pillar to the substrate was $58.6 \pm 5.2 \mu\text{N}$, in excellent agreement with the results obtained with the CMI method ($56.6 \pm 4.5 \mu\text{N}$).

In summary, our FSI method allowed us to measure i) the stiffness of the pillars and ii) the maximum lateral force. From those values it was possible to retrieve iii) the maximum displacement, iv) the maximum stress and v) the adhesion force of the pillars to the substrate. The

Table 1

- Summary of the mechanical parameters of 2PP and EBID nanopillars obtained by CMI method and FSI method. The reported errors are the standard deviation values of the measurements.

	2PP nanopillars		EBID nanopillars		
	CMI method (lateral deflection)	FSI method	CMI method (vertical deflection)	CMI method (lateral deflection)	FSI method
$F_{N,max}^*$ (nN)	1053.7 ± 106	1061.7 ± 135	588.5 ± 69	604.8 ± 36	500.8 ± 48
$F_{N,xy,max}^*$ (nN)	883 ± 89	889.6 ± 113	493.1 ± 58	506.8 ± 30	423.0 ± 40
$h_{residue}$ (nm)	0	0	21.4 ± 1.9	21.4 ± 1.9	35.6 ± 11
$h_{F_{N,xy,max}^*}$ (nm)	530 (apex)	530 (apex)	118.3 ± 1.2	118.3 ± 1.2	127.7 ± 7.8
$d_{pillar,max}$ (nm)	64.2 ± 13	58.4 ± 14	–	–	–
k_{pillar} (N/m)	13.5 ± 3.2	15.9 ± 2.6	–	–	2.4 ± 0.3
σ_{max} (GPa)	0.3 ± 0.03	0.3 ± 0.02	2.8 ± 0.3	2.9 ± 0.2	2.7 ± 0.4
$F_{adh,pillar}$ (μN)	56.6 ± 4.5	58.6 ± 5.2	–	–	–

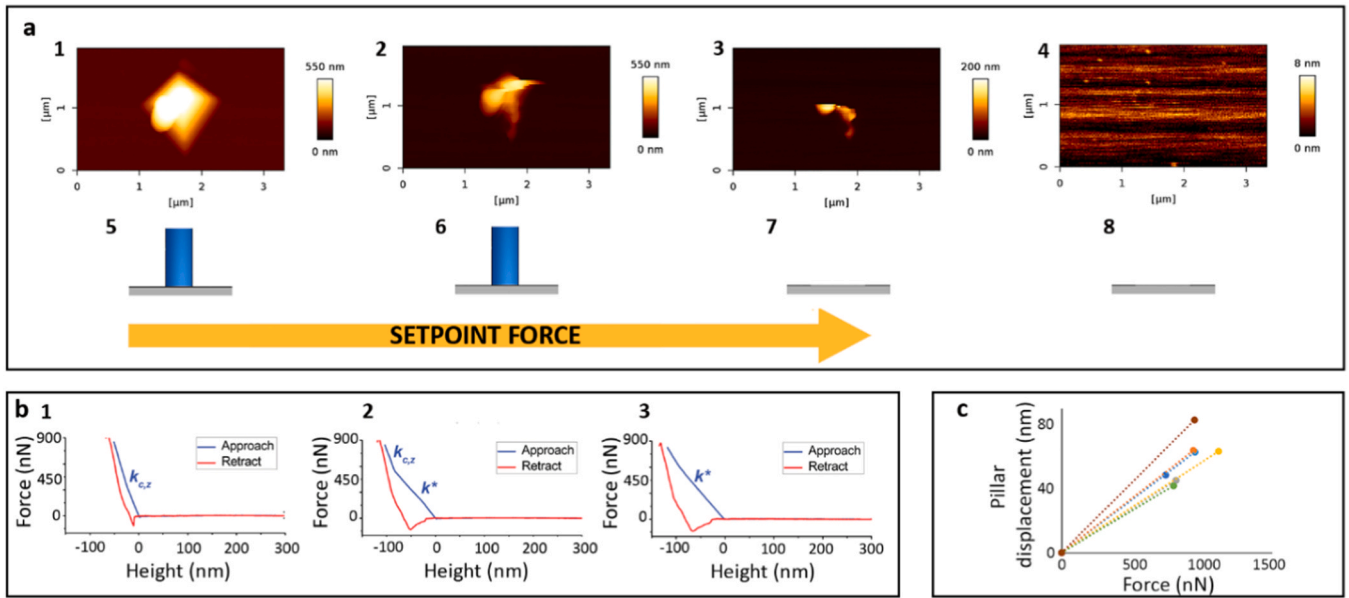


Fig. 5. Mechanical tests performed by FSI on 2PP 3D printed pillars. a) Topography images acquired in QI mode with increasing values of the setpoint force: (a-1) 50 nN, (a-2) 700 nN, (a-3) 800 nN, and (a-4) topography image acquired with low setpoint force (50 nN) after the pillar broke (failure occurred at 800 nN setpoint force), indicating no residue of the pillar. (a-5, a-6, a-7, a-8) schematic morphology of the pillar after each scan. b) Force-distance curves during tip interactions: (b-1) with the substrate, (b-2) with the pillar and subsequently with the substrate and (b-3) only with the pillar without touching the substrate. The approach contact region of the curves acquired with the tip interacting only with the pillar showed a linear trend, indicating a point tip-pillar contact occurring at the apex of the pillar (situation sketched in Fig. 3a-C) and the elastic behavior of the pillar. c) Summary of all the experimental data. The maximum lateral force ($F_{N,xy,max}^*$) and the stiffness of the pillars k_{pillar} (inverse slope of the plot) are deduced from the force curves acquired when the tip was interacting with the pillar without touching the substrate (Fig. b-3), applying Eqs. (31) and (30), respectively. The value of maximum displacement is $d_{pillar,max} = F_{N,xy,max}^*/k_{pillar}$.

quantitative values of all the mechanical parameters are summarized in Table 1. The results are in good agreement with the values obtained with our CMI method.

4.3. EBID Pt/C nanopillars

4.3.1. Mechanical characterization using the CMI method

Mechanical characterization using the CMI method was carried out on 10 nanopillars.

Due to their conical geometry, EBID nanopillars showed a different behavior during the mechanical tests relative to the 2PP pillars.

An example of experiment is reported in Fig. 6a-1–a-18.

When low values of setpoint force (10 nN in the example reported in Fig. 6a-1–a-6) were applied, a slight decrease of the height of the pillar was observed in QI mode images acquired after CMI scans (252 nm in the reported example, see corresponding height profile in Fig. 6b-1), meaning that the fracture of the pillar occurred at a section very close to the apex of the pillar. This behavior is coherent with the stress distribution in a “sharp” conical pillar with a lateral force applied at its apex, where the height of the maximum stress is closer to the apex of the pillar, the tinier the tip of the pillar is [59].

Indeed, referring to Fig. 6b-2, the maximum bending stress (which is in the section corresponding to the height of the residue of the pillar, where the fracture occurs), can be written as:

$$\sigma_{max}(z) = \frac{MR_{res}}{I} = 4 \frac{F_{N,xy,max}^* z}{\pi R_{res}^3} \quad (35)$$

where R_{res} is the radius of the section of the cone corresponding to the height of the residue, which is:

$$R_{res} = R_{apex} + (\Delta h_{F_{N,xy,max}^*} + z) \tan \alpha \quad (36)$$

with α the half cone angle of the pillar and z the distance between the point of application of the force and the height of the residue.

Calculating the derivative of the $\sigma_{max}(z)$ and equating it to zero:

$$\frac{d\sigma_{max}(z)}{dz} = 0, \quad (37)$$

we obtain the equation for the distance z between the point of application of the force and the most stressed section:

$$z = \frac{R_{apex} + \Delta h_{F_{N,xy,max}^*} \tan \alpha}{2 \tan \alpha} = \frac{R_{apex} + (h_{pillar} - h_{F_{N,xy,max}^*}) \tan \alpha}{2 \tan \alpha} \quad (38)$$

This relationship tells us that the most stressed section is as closer to the point of application of the force ($z \rightarrow 0$) as sharper is the tip of the pillar ($R_{apex} \rightarrow 0$) and as closer to the apex of the pillar is the point of application of the lateral force ($h_{F_{N,xy,max}^*} \rightarrow h_{pillar}$).

By further increasing the setpoint force we observed the fracture of the pillars occurring at a significantly lower height. For instance, in the example reported in Fig. 6, a residue of about 150 nm in height was observed (Fig. 6b-1) when a setpoint force of 90 nN was applied (Fig. 6a-7–a-12) and a residue of about 20 nm in height (Fig. 6b-1) was observed when a setpoint of 100 nN was applied. (Fig. 6a-13–a-18). This can only be due to the fact that the lateral force was applied at a lower point possibly as a result of: i) the previous breakage of the tip of the pillar, *i.e.*, the lowest height of the truncated pillar; ii) the resting of the AFM tip against the sidewall of the deformed pillar, which could further lower the application point of the force.

The use of the data acquired when the pillars broke very close to their apex were not convenient for the calculation of the mechanical parameters of the pillars, *e.g.*, the maximum stress, because of two reasons: i) the breakage of the pillars was not easily visible while performing the experiments and the height of the pillars had to be precisely measured after each applied force level; ii) the distance (z) between the application point of the force and the most stressed section (important to accurately calculate the maximum stress, as showed by Eq. 35) was in the order of few nm, *i.e.*, the same order of magnitude as the AFM topography accuracy on these kinds of structures, and therefore it was considered not measurable with enough accuracy.

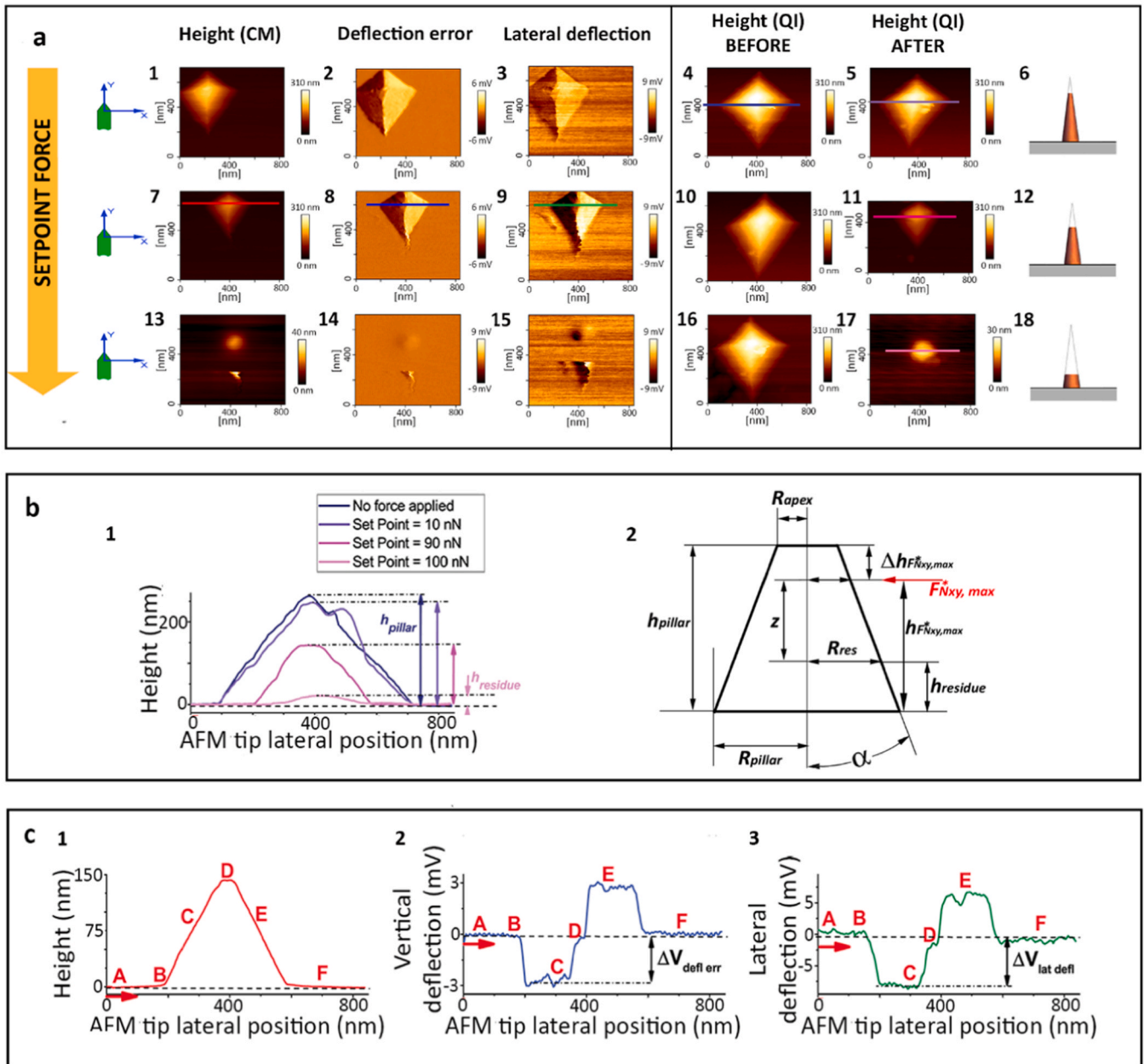


Fig. 6. Mechanical tests performed by using the CMI method on EBID nanopillars. a) AFM images acquired during the test on a single pillar: topography (a-1, a-2, a-7, a-13), deflection error (a-2, a-8, a-14) and lateral deflection (a-3, a-9, a-15) images acquired in contact mode with increasing values of the setpoint forces (10 nN, 90 nN, 100 nN). Before (a-4, a-10, a-16) and after (a-5, a-11, a-17) the application of each setpoint force level, the morphology of the pillars was checked by acquiring new topography images in QI mode with low setpoint force. The morphology after the application of each setpoint value is sketched in a-6, a-12, a-18. b-1) Height profiles obtained by QI topography images acquired after the application of each force level (sections of the pillar evidenced in figures a-4, a-5, a-11, a-17), where the variation of the height of the pillar can be observed. h_{pillar} is the initial height of the nanopillar (260 nm), $h_{residue}$ (26 nm) is the height of the residue at the force level used for the calculation of the maximum stress of the pillar. b-2) Sketch of a generic pillar with conical shape with a lateral force $F_{N,xy,max}^*$ applied at a certain height $h_{F_{N,xy,max}^*}$. We indicated with h_{pillar} the height of the pillar, $h_{residue}$ the height of the residue of the pillar after breakage, z the distance between the point of application of the force $F_{N,xy,max}^*$ and the height of the residue, R_{pillar} the radius of the base of the pillar and R_{apex} , the radius of the apex of the pillar. c) Line graphs across the pillar: height (c-1), vertical deflection error (c-2) and lateral deflection (c-3) profiles corresponding to the sections of the pillar evidenced in figures a-7, a-8 and a-9, respectively.

Therefore, we considered convenient, in order to make the measurement procedure easier and more accurate, to use values of the applied force high enough to produce the fracture of the pillar at a lower (visible and accurately measurable) height. This was possible because the increase of the value of the force used to break the conical pillar and the consequent decrease of its application height ($h_{F_{N,xy,max}^*}$) did not affect the measured value of the maximum stress, but only lowered the height of the most stressed section. Indeed, according to Eqs. (35)–(37),

the maximum stress depends only on the value of the lateral force $F_{N,xy,max}^*$, the height of application of the force, the distance (z) between the height of application of the lateral force and the height of most stressed section (i.e., the height of the residue), and the initial geometry of the pillar (i.e., R_{apex} and the aperture angle α).

We easily observed the fracture of the nanopillars (with residues of about 20 nm height) by applying setpoint forces in the range 90–120 nN and we applied this range of setpoint forces to 10 nanopillars to retrieve

the maximum stress.

In Fig. 6c, example profiles of the height (Fig. 6c-1), vertical deflection error (Fig. 6c-2) and lateral deflection (Fig. 6c-3) recorded at 90 nN setpoint force (cross-sections highlighted as colored lines in Fig. 6a-7, a-8, a-9) are reported. The trend of these profiles were coherent with the expected trends and similar to those observed for the 3D printed pillars.

For each pillar, the applied force (F^*_{N}) and its lateral component $F^*_{N,xy}$ were calculated in two different ways: i) from the vertical deflection signal, by applying Eqs. (15) and (22), and ii) from the lateral deflection signal, by applying Eqs. (16) and (22). The average value of the lateral rupture force $F^*_{N,xy,max}$ (i.e., the lateral component of the force corresponding to the setpoint force at which the visible rupture of the pillars was observed) was 493.1 ± 58.0 nN, calculated from the vertical deflection signal, and 506.8 ± 30.3 nN, calculated from the lateral deflection signal. The good agreement between the results obtained from the two different signals confirms the validity of both calculation methods.

From the topography images acquired in QI mode with low setpoint force (10 nN) after the breakage of the pillars, we were able to measure the height of residue, i.e., the height of the most stressed section (where the fracture occurred) in the tested experimental conditions. For the tested pillars, an average residue height of 21.4 ± 1.9 nm was found.

The height of the application of the lateral force can be analytically calculated by using Eq. (38) and, interestingly, depends only on the height of the residue of the broken pillar (and its geometrical parameters). Indeed, the distance z between the point of application of the lateral force and the most stressed section (at the height of the residue of the pillar) can be written as

$$z_{omax} = h_{F^*_{N,xy,max}} - h_{res} \quad (39)$$

with $h_{F^*_{N,xy,max}}$ the height of application of the force $F^*_{N,xy,max}$ and h_{res} the measured height of the residue of the pillar.

Therefore, we could obtain the height of the application of the force, which was:

$$h_{F^*_{N,xy,max}} = \frac{1}{3} \frac{R_{apex}(h_{pillar} + 2h_{res})}{\tan\alpha} \quad (40)$$

where we considered $R_{apex} = 5$ nm (estimated by SEM images).

By using this relationship, we calculated the height of the application of the lateral force of each analyzed nanopillar and we found an average height of 118.3 ± 1.2 nm.

We finally calculated the maximum bending stress, corresponding to the section where the fracture occurred through Eq. (35) and we found a value of 2.8 ± 0.3 GPa and 2.9 ± 0.2 GPa considering the lateral force calculated from the vertical deflection signal and from the lateral deflection signal, respectively. The compression stress due to the vertical component of the applied force $F_{N,z}$ and the stress due to capillarity were not taken into account, being negligible (1–2 orders of magnitude lower than the bending stress).

It is worth noting that, differently from the previous case of the 2PP 3D printed pillars, no detachment of the pillars from the substrate was observed, but real fractures of the material. Therefore, this value of maximum stress can be assumed as the fracture stress of the Pt-C EBID deposited material.

To our knowledge, no other data on the fracture stress of the same Pt-C EBID nanopillars are available in the literature, but the values we found are in line with the stress values measured by other authors on bigger structures fabricated by EBID using different precursors (in the range 1–3 GPa) [61].

In summary, our CMI method allowed us to successfully characterize the maximum stress of the conical EBID nanopillars. Indeed, it enabled us to apply a controlled lateral force which produced the fracture at a certain measurable height. These two parameters ($F^*_{N,xy,max}$ and h_{res}) allowed us to determine the maximum stress for the analyzed structures.

Those values are summarized in Table 1 and are compared with the same parameters obtained by FSI method (described in the following paragraph).

4.3.2. Mechanical characterization using the FSI method

Equivalent mechanical characterization (determination of the maximum stress) of the same EBID nanopillars was carried out using our alternative FSI method. This allowed us to compare again the results obtained with the two methods and corroborate them. Eight nanopillars were analyzed by using this method.

In Fig. 7, the topography images of 2 pillars subjected to increasing values of setpoint force are shown. At low values of setpoint force (10 nN in the example reported in Fig. 7a-1), no changes in the morphology of the pillars were noticed, meaning that no fracture of the pillars occurred. Similar to what we observed in the CMI, at higher values of setpoint force (e.g., 100 nN in the example reported in Fig. 7a-2), a very small decrease of the height of the nanopillars was observed (about 5 nm), coherent with the conical geometry (see Eq. 38). By further increasing the setpoint force (300 nN in the example reported in Fig. 7a-3), we observed the fracture of the pillars occurring at a lower and more visible height. This was mainly because increasing the setpoint force we made the tip to rest against the pillar sidewall, lowering the actual point of application of the force. Similar to the methodology applied in the CMI, to improve the ease and the accuracy of the measurements, we focused on these values of applied force, i.e., high enough to produce the breakage of the pillar at a lower height (e.g., h_{res} showed in Fig. 7b).

The range of setpoint forces in which the pillars were observed to break at a low and visible height was 260–320 nN.

In Fig. 7c, examples of force-distance curves acquired in different points along the section of a nanopillar are shown. Since the substrate was rigid (Si wafer), the curves acquired on the substrate (Fig. 7c-1) exhibited, as expected, a slope of the contact region equal to the stiffness of the cantilever. In the first scan points where the AFM tip touched the pillars, the contact region of the approach curves presented two different slopes (Fig. 7c-2), corresponding to: i) the equivalent stiffness of the system “cantilever+pillar” k^* at low force values and ii) the stiffness of the cantilever at high force values, indicating the tip touching the substrate.

In Fig. 7c-3, a typical curve registered when the AFM probe was interacting only with the pillar is reported. Different from the case of the 3D printed cylindrical polymeric pillars, the slope of the contact region of the approach curve was observed to be not constant in the entire range of force values. At the very beginning (low force values), the curve appeared linear, indicating a point contact between the sidewall of the AFM tip and the apex of the pillar (situation sketched in Fig. 1c-c). From the slope of this region, it was, therefore, possible to retrieve the stiffness of the pillars using Eq. (31), which resulted in a value of 2.4 ± 0.3 N/m (the average value of three curves for each pillar was considered). Nevertheless, it is worth noting that this value cannot be assumed as the value of the stiffness of the pillars, since probably a part of the tip of the pillar was already broken due to the previously applied levels of force. After a certain force value, the slope of the curve starts to progressively increase, indicating that the AFM tip rests against the deformed pillar and starts to glide along its lateral wall (situation sketched in Fig. 1c-D). This result is coherent with the findings obtained with our CMI method.

As previously explained, in this case, the value of applied force can be calculated by using Eq. (32), considering the slope of the very last part of the approaching F-d curve (k^*_{app}). We obtained an average value of applied lateral force at breakage $F^*_{N,xy,max}$ of 423.0 ± 40.7 nN for the analyzed pillars. This value of force is slightly lower than the values of maximum lateral force obtained by our CMI method on the same nanopillars, but the results are coherent if we look at the height of the pillars residues. Indeed, topography images acquired with low setpoint force after pillars fracture revealed the presence of a residue that was slightly taller than that one observed with CMI method, i.e., 35.6 ± 11.6 nm. This indicates a different position of the application

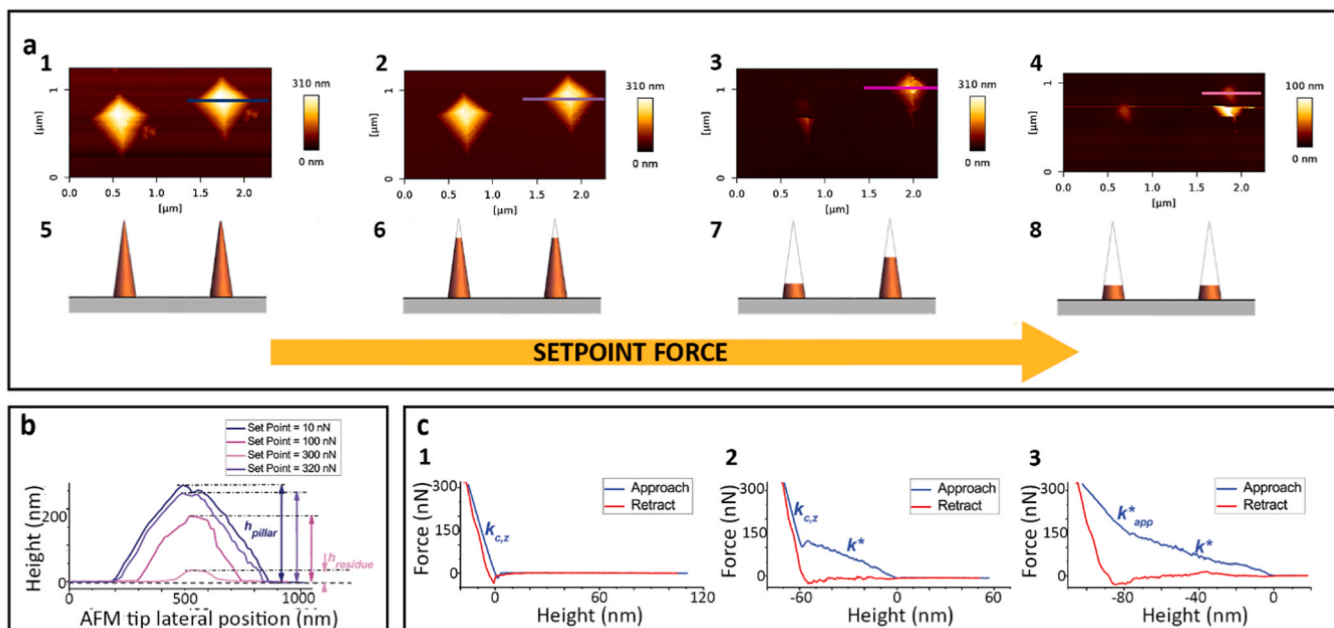


Fig. 7. Mechanical tests performed by the FSI on EBID nanopillars. a) Topography images acquired in QI mode with increasing values of setpoint force: (a-1) 10 nN, (a-2) 100 nN, (a-3) 300 nN and (a-4) 320 nN. (a-5, a-6, a-7, a-8) schematics of the morphology of the nanopillars observed after each scan. b) Height profiles of the pillar recorded at each setpoint force level. The corresponding sections are shown in Fig. a-1, a-2, a-3 and a-4. h_{pillar} is the initial height of the pillar and $h_{residue}$ is the height of the residue at the force level that was used for the calculation of the maximum stress (setpoint force of 320 nN in this case). c) Force-distance curves acquired with: (c-1) the tip on the substrate, (c-2) the tip in contact with the pillar and eventually with the substrate and (c-3) the tip in contact only with the pillar without touching the substrate. The approach contact region of the curves acquired with the tip interacting only with the pillar showed a progressive increase of the slope, indicating that the AFM tip slides along the sidewall of the tip (as shown in Fig. 3a-D).

point of the lateral force.

We calculated the height of application of the lateral force of each analyzed nanopillar using Eq. (40) and we found an average height of 127.7 ± 7.8 nm, as expected, slightly higher than the height of the force found in the CMI experiments.

We finally calculated the maximum stress, corresponding to the section where the fracture occurred and we found a value of 2.7 ± 0.4 GPa, comparable with the values of maximum stress obtained using our CMI method and with the few data available in the literature for different EBID structures deposited with different precursors [61]. It is worth noting that the compression stress due to the vertical component of the applied force $F_{N,z}$ and the stress due to capillarity were negligible and were not taken into account for the estimation of the maximum stress.

In summary, our FSI method allowed us to measure the maximum stress, similar to the CMI method. The very good agreement between the values of maximum stress found with FSI method and CMI method (see the comparative Table 1) represents further evidence of the suitability of our AFM based methods for the mechanical characterization of nanopillars.

5. Conclusion

In this work, we have proposed two methods to perform mechanical tests on single nanopillars, addressing the need for novel mechanical characterization methodologies accessible and easy to be performed for this kind of structures without sample modification. The proposed methods are based on the sole use of AFM in the contact mode imaging (CMI) and force spectroscopy imaging (FSI) mode. They do not involve modification of the samples and allow for the quantification of the elastic properties of the structures and of their breaking strength (i.e., maximum force, maximum displacement, most loaded section).

The effective operation of the two methods was demonstrated by two case studies: i) polymeric nanopillars fabricated by two-photon

polymerization (2PP) and ii) Pt-C nanopillars fabricated by electron beam induced deposition (EBID). In the case of the cylindrical 2PP nanopillars, the stiffness, the elastic modulus, the maximum lateral force, the maximum displacement, the maximum stress and the adhesion force of the pillars to the substrate were measured by both methods (i.e., CMI and FSI). In the case of the conical EBID nanopillars, the maximum stress of the nanopillars was determined by CMI and FSI method. A high consistency of all the results obtained with our two methods was observed.

The novel CMI and FSI methods were validated by comparing the elastic modulus values of 2PP pillars with the elastic modulus value obtained by the well-established Quantitative Imaging (QI) mode. We determined an accuracy of 3.3% for CMI method and 13.8% for FSI. The precision of both CMI and FSI methods (coefficient of variation of 21% and 17.7%, respectively), was similar to the precision of the conventional QI mode (18%). In addition, the validity of our methods was further demonstrated by the consistency of our results with the parameters analytically calculated.

In summary, we developed two effective AFM based methods for the mechanical characterization of single nanopillars, that do not require the use of SEM and/or additional sample modification. The proposed methodologies are easy to use and could be beneficial for fabrication and optimization of micro and nanopatterned surfaces. Furthermore, they have the potential of enabling otherwise impossible measurements, particularly when the specimens need to be tested under wet conditions, such as in the case of mechanobiological studies involving living cells.

CRediT authorship contribution statement

L.A., with the supervision of M.K.G. and L.E.F-A., designed the AFM procedures, the experiments and the concept of the manuscript. M.G. fabricated the EBID nanopillars and carried out SEM characterization of the EBID samples and AFM probes, under the supervision of C.W.H. and L.E.F-A. M.N.G. fabricated the 2PP nanopillars, under the supervision of

L.E.F-A. and A.A.Z. L.A. performed the AFM experiments. L.A., M.J.M., M.K.G. and L.E.F-A analyzed the results. L.A. wrote the draft of the manuscript, which was revised by all the authors. All authors have approved the final version of the manuscript.

Declaration of Competing Interest

The authors declare that they have no known competing financial interests or personal relationships that could have appeared to influence the work reported in this paper.

Acknowledgements

This research has received funding from the TU Delft 'Diagnosis' of soft matter on nanopatterned surfaces for better implants Cohesion Grant 'Diagnosis' of soft matter on nanopatterned surfaces for better implants and from the European Union's Horizon 2020 research and innovation program under the Marie Skłodowska Curie grant agreement No 707404.

Appendix A. Supporting information

Supplementary data associated with this article can be found in the online version at doi:10.1016/j.addma.2021.101858.

References

- 1] E. Menard, M.A. Meitl, Y.G. Sun, J.U. Park, D.J.L. Shir, Y.S. Nam, S. Jeon, J. A. Rogers, Micro- and nanopatterning techniques for organic electronic and optoelectronic systems, *Chem. Rev.* 107 (4) (2007) 1117–1160.
- 2] G.P. Luo, X.G. Ren, S. Zhang, H.B. Wu, W.C.H. Choy, Z.C. He, Y. Cao, Recent advances in organic photovoltaics: device structure and optical engineering optimization on the nanoscale, *Small* 12 (12) (2016) 1547–1571.
- 3] C. Cottin-Bizonne, J.L. Barrat, L. Bocquet, E. Charlaix, Low-friction flows of liquid at nanopatterned interfaces, *Nat. Mater.* 2 (4) (2003) 237–240.
- 4] P. Pendyala, H.S. Grewal, H.N. Kim, L.J. Cho, E.S. Yoon, Individual role of the physicochemical characteristics of nanopatterns on tribological surfaces, *ACS Appl. Mater. Interfaces* 8 (44) (2016) 30590–30600.
- 5] C. Corbella, S. Portal-Marco, M. Rubio-Roy, E. Bertran, G. Oncins, M.A. Vallve, J. Ignés-Mullol, J.L. Andujar, Modifying surface properties of diamond-like carbon films via nanotexturing, *J. Phys. D Appl. Phys.* 44 (39) (2011), 395301.
- 6] J.Y. Lim, H.J. Donahue, Cell sensing and response to micro- and nanostructured surfaces produced by chemical and topographic patterning, *Tissue Eng.* 13 (8) (2007) 1879–1891.
- 7] S. Dobbenga, L.E. Fratila-Apachitei, A.A. Zadpoor, Nanopattern-induced osteogenic differentiation of stem cells - a systematic review, *Acta Biomater.* 46 (2016) 3–14.
- 8] K. Zhang, X.F. Xiao, X.M. Wang, Y.B. Fan, X.M. Li, Topographical patterning: characteristics of current processing techniques, controllable effects on material properties and co-cultured cell fate, updated applications in tissue engineering, and improvement strategies, *J. Mater. Chem. B* 7 (45) (2019) 7090–7109.
- 9] K. Anselme, P. Davidson, A.M. Poppa, M. Giazzon, M. Liley, L. Ploux, The interaction of cells and bacteria with surfaces structured at the nanometre scale, *Acta Biomater.* 6 (10) (2010) 3824–3846.
- 10] M. Ganjian, K. Modaresifar, M.R.O. Ligeon, L.B. Kunkels, N. Turner, L. Angeloni, C. W. Hagen, L.C. Otten, P.L. Hagedoorn, I. Apachitei, L.E. Fratila-Apachitei, A. A. Zadpoor, Nature helps: toward bioinspired bactericidal nanopatterns, *Adv. Mater. Interfaces* 6 (16) (2019), 1900640.
- 11] M. Nouri-Goushki, M.J. Mirzaali, L. Angeloni, D. Fan, M. Minneboo, M. K. Ghatkesar, U. Stauffer, L.E. Fratila-Apachitei, A.A. Zadpoor, 3D printing of large areas of highly ordered submicron patterns for modulating cell behavior, *ACS Appl. Mater. Interfaces* 12 (1) (2020) 200–208.
- 12] K. Modaresifar, S. Azizian, M. Ganjian, L.E. Fratila-Apachitei, A.A. Zadpoor, Bactericidal effects of nanopatterns: a systematic review, *Acta Biomater.* 83 (2019) 29–36.
- 13] K.K. Chung, J.F. Schumacher, E.M. Sampson, R.A. Burne, P.J. Antonelli, A. B. Brennana, Impact of engineered surface microtopography on biofilm formation of *Staphylococcus aureus*, *Biointerphases* 2 (2) (2007) 89–94.
- 14] D.P. Linklater, S. Juodkazis, S. Rubanov, E.P. Ivanova, Comment on "bactericidal effects of natural nanopatterning of dragonfly wing on *Escherichia coli*", *ACS Appl. Mater. Interfaces* 9 (35) (2017) 29387–29393.
- 15] S. Ghosh, S.Y. Niu, M. Yankovska, M. Mecklenburg, S.M. King, J. Ravichandran, R. K. Kalia, A. Nakano, P. Vashishta, P. Setlow, Analysis of killing of growing cells and dormant and germinated spores of *Bacillus* species by black silicon nanopillars, *Sci. Rep.* 7 (2017) 17768.
- 16] A.J. Engler, S. Sen, H.L. Sweeney, D.E. Discher, Matrix elasticity directs stem cell lineage specification, *Cell* 126 (4) (2006) 677–689.
- 17] J.H. Wen, L.G. Vincent, A. Fuhrmann, Y.S. Choi, K.C. Hribar, H. Taylor-Weiner, S. C. Chen, A.J. Engler, Interplay of matrix stiffness and protein tethering in stem cell differentiation, *Nat. Mater.* 13 (10) (2014) 979–987.
- 18] M. Guevendien, J.A. Burdick, Stiffening hydrogels to probe short- and long-term cellular responses to dynamic mechanics, *Nat. Commun.* 3 (2012) 792.
- 19] S. Rahmouni, A. Lindner, F. Rechenmacher, S. Neubauer, T.R.A. Sobahi, H. Kessler, E.A. Cavalcanti-Adam, J.P. Spatz, Hydrogel micropillars with integrin selective peptidomimetic functionalized nanopatterned tops: a new tool for the measurement of cell traction forces transmitted through $\alpha(v)\beta(3)$ -or $\alpha(5)\beta(1)$ -Integrins, *Adv. Mater.* 25 (41) (2013) 5869–5874.
- 20] M. Gupta, L. Kocgozlu, B.R. Sarangi, F. Margadant, M. Ashraf, B. Ladoux, Micropillar substrates: a tool for studying cell mechanobiology, *Method Cell Biol.* 125 (2015) 289–308.
- 21] F. Deng, W.B. Lu, H.B. Zhao, Y.T. Zhu, B.S. Kim, T.W. Chou, The properties of dry-spun carbon nanotube fibers and their interfacial shear strength in an epoxy composite, *Carbon* 49 (5) (2011) 1752–1757.
- 22] L.X. Zheng, G.Z. Sun, Z.Y. Zhan, Tuning array morphology for high-strength carbon-nanotube fibers, *Small* 6 (1) (2010) 132–137.
- 23] M.F. Yu, O. Lourie, M.J. Dyer, K. Moloni, T.F. Kelly, R.S. Ruoff, Strength and breaking mechanism of multiwalled carbon nanotubes under tensile load, *Science* 287 (5453) (2000) 637–640.
- 24] A.H. Barber, R. Andrews, L.S. Schadler, H.D. Wagner, On the tensile strength distribution of multiwalled carbon nanotubes, *Appl. Phys. Lett.* 87 (20) (2005), 203106.
- 25] E. Zussman, X. Chen, W. Ding, L. Calabri, D.A. Dikin, J.P. Quintana, R.S. Ruoff, Mechanical and structural characterization of electrospun PAN-derived carbon nanofibers, *Carbon* 43 (10) (2005) 2175–2185.
- 26] I. Kaplan-Ashiri, S.R. Cohen, K. Gartsman, V. Ivanovskaya, T. Heine, G. Seifert, I. Wiesel, H.D. Wagner, R. Tenne, On the mechanical behavior of WS2 nanotubes under axial tension and compression, *Proc. Natl. Acad. Sci. U.S.A.* 103 (3) (2006) 523–528.
- 27] N.N. Nemeth, L.J. Evans, O.M. Jadaon, W.N. Sharpe, G.M. Beheim, M.A. Trapp, Fabrication and probabilistic fracture strength prediction of high-aspect-ratio single crystal silicon carbide microspecimens with stress concentration, *Thin Solid Films* 515 (6) (2007) 3283–3290.
- 28] Y. Zhu, F. Xu, Q.Q. Qin, W.Y. Fung, W. Lu, Mechanical properties of vapor-liquid-solid synthesized silicon nanowires, *Nano Lett.* 9 (11) (2009) 3934–3939.
- 29] D. Kiener, W. Grosinger, G. Dehm, R. Pippan, A further step towards an understanding of size-dependent crystal plasticity: in situ tension experiments of miniaturized single-crystal copper samples, *Acta Mater.* 56 (3) (2008) 580–592.
- 30] Y.H. Yue, N.K. Chen, X.B. Li, S.B. Zhang, Z. Zhang, M.W. Chen, X.D. Han, Crystalline liquid and rubber-like behavior in Cu nanowires, *Nano Lett.* 13 (8) (2013) 3812–3816.
- 31] F. Ostlund, K. Rzepiejewska-Malyska, K. Leifer, L.M. Hale, Y.Y. Tang, R. Ballarini, W.W. Gerberich, J. Michler, Brittle-to-ductile transition in uniaxial compression of silicon pillars at room temperature, *Adv. Funct. Mater.* 19 (15) (2009) 2439–2444.
- 32] A.T. Jennings, M.J. Burek, J.R. Greer, Microstructure versus size: mechanical properties of electroplated single crystalline Cu nanopillars, *Phys. Rev. Lett.* 104 (13) (2010), 135503.
- 33] J.R. Greer, J.Y. Kim, M.J. Burek, The in-situ mechanical testing of nanoscale single-crystalline nanopillars, *JOM* 61 (12) (2009) 19–25.
- 34] B.B. Lewis, B.A. Mound, B. Srijanto, J.D. Fowlkes, G.M. Pharr, P.D. Rack, Growth and nanomechanical characterization of nanoscale 3D architectures grown via focused electron beam induced deposition, *Nanoscale* 9 (42) (2017) 16349–16356.
- 35] A. Banerjee, D. Bernoulli, H.T. Zhang, M.F. Yuen, J.B. Liu, J.C. Dong, F. Ding, J. Lu, M. Dao, W.J. Zhang, Y. Lu, S. Suresh, Ultralarge elastic deformation of nanoscale diamond, *Science* 360 (6386) (2018) 300–302.
- 36] S. Hoffmann, I. Utke, B. Moser, J. Michler, S.H. Christiansen, V. Schmidt, S. Senz, P. Werner, U. Gosele, C. Ballif, Measurement of the bending strength of vapor-liquid-solid grown silicon nanowires, *Nano Lett.* 6 (4) (2006) 622–625.
- 37] S. Okada, T. Mukawa, R. Kobayashi, M. Ishida, Y. Ochiai, T. Kaito, S. Matsui, J. Fujita, Comparison of Young's modulus dependency on beam accelerating voltage between electron-beam- and focused ion-beam-induced chemical vapor deposition pillars, *Jpn. J. Appl. Phys.* 45 (6b) (2006) 5556–5559.
- 38] V. Friedli, I. Utke, K. Molhave, J. Michler, Dose and energy dependence of mechanical properties of focused electron-beam-induced pillar deposits from Cu (C5HF6O2)2, *Nanotechnology* 20 (38) (2009), 385304.
- 39] T. Namazu, Y. Isono, T. Tanaka, Evaluation of size effect on mechanical properties of single crystal silicon by nanoscale bending test using AFM, *J. Microelectromech. Syst.* 9 (4) (2000) 450–459.
- 40] X.D. Li, B. Bhushan, Fatigue studies of nanoscale structures for MEMS/NEMS applications using nanoindentation techniques, *Surf. Coat. Tech.* 163 (2003) 521–526.
- 41] S. Sundararajan, B. Bhushan, Development of AFM-based techniques to measure mechanical properties of nanoscale structures, *Sens. Actuators A Phys.* 101 (3) (2002) 338–351.
- 42] Y.J. Kim, K. Son, I.C. Choi, I.S. Choi, W.I. Park, J.I. Jang, Exploring nanomechanical behavior of silicon nanowires: AFM bending versus nanoindentation, *Adv. Funct. Mater.* 21 (2) (2011) 279–286.
- 43] M. Maksud, M. Barua, M.R.A. Shikder, B.W. Byles, E. Pomerantseva, A. Subramanian, Tunable nanomechanical performance regimes in ceramic nanowires, *Nanotechnology* 30 (47) (2019) 47LT02.
- 44] M. Antsov, B. Polyakov, V. Zadin, M. Mets, S. Oras, M. Vahtrus, R. Lohmus, L. Dorogin, S. Vlassov, Mechanical characterisation of pentagonal gold nanowires in three different test configurations: a comparative study, *Micron* 124 (2019), 102686.

- [45] J. Zhou, Q. Cai, X. Liu, Y.H. Ding, F. Xu, Temperature effect on the mechanical properties of electrospun PU nanofibers, *Nanoscale Res. Lett.* 13 (2018) 384.
- [46] A. Morel, S. Domaschke, V.U. Kumaran, D. Alexeev, A. Sadeghpour, S. N. Ramakrishna, S.J. Ferguson, R.M. Rossi, E. Mazza, A.E. Ehret, G. Fortunato, Correlating diameter, mechanical and structural properties of poly(L-lactide) fibres from needleless electrospinning, *Acta Biomater.* 81 (2018) 169–183.
- [47] M.J. Gordon, T. Baron, F. Dhalluin, P. Gentile, P. Ferret, Size effects in mechanical deformation and fracture of cantilevered silicon nanowires, *Nano Lett.* 9 (2) (2009) 525–529.
- [48] R. Helling, A. Mieth, S. Altmann, T.J. Simat, Determination of the overall migration from silicone baking moulds into simulants and food using 1H NMR techniques, *Food Addit. Contam. A* 26 (3) (2009) 395–407.
- [49] G. Binnig, C.F. Quate, C. Gerber, Atomic force microscope, *Phys. Rev. Lett.* 56 (9) (1986) 930–933.
- [50] D. Passeri, A. Alippi, A. Bettucci, M. Rossi, E. Tamburri, M.L. Terranova, Indentation modulus and hardness of polyaniline thin films by atomic force microscopy, *Synth. Met.* 161 (1–2) (2011) 7–12.
- [51] R. Garcia, Nanomechanical mapping of soft materials with the atomic force microscope: methods, theory and applications, *Chem. Soc. Rev.* 49 (2020) 5850–5884.
- [52] L. Angeloni, M. Reggente, D. Passeri, M. Natali, M. Rossi, Identification of nanoparticles and nanosystems in biological matrices with scanning probe microscopy, *Wiley Interdiscip. Rev. Nanomed. Nanobiotechnol.* 10 (6) (2018), e1521.
- [53] C.R. Guerrero, P.D. Garcia, R. Garcia, Subsurface imaging of cell organelles by force microscopy, *ACS Nano* 13 (8) (2019) 9629–9637.
- [54] M. Reggente, D. Passeri, L. Angeloni, F.A. Scaramuzza, M. Barteri, F. De Angelis, I. Persiconi, M.E. De Stefano, M. Rossi, Detection of stiff nanoparticles within cellular structures by contact resonance atomic force microscopy subsurface nanomechanical imaging, *Nanoscale* 9 (17) (2017) 5671–5676.
- [55] J.E. Sader, I. Larson, P. Mulvaney, L.R. White, Method for the calibration of atomic force microscope cantilevers, *Rev. Sci. Instrum.* 66 (7) (1995) 3789–3798.
- [56] J.E. Sader, J.R. Friend, Note: calibration of atomic force microscope cantilevers using only their resonant frequency and quality factor, *Rev. Sci. Instrum.* 85 (11) (2014), 116101.
- [57] M.L.B. Palacio, B. Bhushan, Normal and lateral force calibration techniques for AFM cantilevers (vol 35, pg 73, 2010), *Crit. Rev. Solid State* 35 (3) (2010), 261–261.
- [58] M. Ganjian, L. Angeloni, M.J. Mirzaali, K. Modaresifar, C.W. Hagen, M. K. Ghatkesar, P.L. Hagedoorn, L.E. Fratila-Apachitei, A.A. Zadpoor, Quantitative mechanics of 3D printed nanopillars interacting with bacterial cells, *Nanoscale* 12 (43) (2020) 21988–22001.
- [59] J. Purto, A. Verch, P. Rogin, R. Hensel, Improved development procedure to enhance the stability of microstructures created by two-photon polymerization, *Microelectron. Eng.* 194 (2018) 45–50.
- [60] I. Utke, J. Michler, R. Winkler, H. Plank, Mechanical properties of 3D nanostructures obtained by focused electron/ion beam-induced deposition: a review, *Micromachines* 11 (4) (2020) 397.
- [61] M.J. Mirzaali, A. Herranz de la Nava, D. Gunashekar, M. Nouri-Goushki, R.P. E. Veeger, Q. Grossman, L. Angeloni, M.K. Ghatkesar, L.E. Fratila-Apachitei, E.L. D. RuffoniDoubrovski, A.A. Zadpoor, Mechanics of bioinspired functionally graded soft-hard composites made by multi-material 3D printing, *Compos. Struct.* 237 (2020) 111867.